1

2

3

4

5   Thermo-poro-mechanical analysis of landslides: from creeping behaviour to catastrophic

6   failure

7   E. E. Alonso [1], A. Zervos [2], N.M. Pinyol [1,3]

8   (1): Department of Geotechnical Engineering and Geosciences, UPC, Barcelona

9   (2): Faculty of Engineering and the Environment, University of Southampton

10   (3): International Center for Numerical Methods in Engineering

11

12

13   Corresponding Author: Eduardo E. Alonso

14   eduardo.alonso@upc.edu

15

16

17

18   ABSTRACT

19   Catastrophic landslides are characterized by high velocities (1 to 100 m/s), large displacements

20   (tens to hundreds of meters) and, in most cases, by a large mobilized mass, in excess of $1Mm^3$.

21   The scope of the paper encompasses planar and compound sliding motions which may exhibit

22   creeping behaviour during a certain period but may evolve to a very rapid motion. Thermo-

23   mechanical interactions, at the scale of the sliding surface, are accepted as a critical aspect to

24   explain these motion phases and their relationship.

25   The paper reviews the mechanisms leading to strength reduction of the failure surface and the

26   published thermo-mechanical formulations. They share a common basic structure. The sliding

27   kinetics and global equilibrium are described at a large scale (the landslide itself) and the

28   evolving shearing strength at the sliding surface derives from the "local" analysis of the

29   shearing band and its vicinity. Pore pressures, temperatures and related variables are

30   estimated by resolving a set of balance equations. Both scales are fully coupled. A significant

31   aspect analyzed in detail in the paper is the transition from creeping motions to a rapid event.

32   It requires the joint consideration of strain-rate effects on friction and the thermo-poro-

33   mechanical analysis of the shearing band and its vicinity. Results are found in terms of

34   dimensionless numbers which control the entire phenomenon. Calculation of the slide

35   evolution requires special numerical techniques described in the paper. Band permeability is

36   found to be the dominant property controlling the triggering of fast motions. The creeping

37   stage and the eventual slide blowup are intimately linked. This relationship is explored in the

38   paper.

39   Although this is not pursued in this paper, the models presented can be readily used to back-

40   analyse relevant case histories or, in principle, even to carry out predictive modelling, provided

41   an adequate calibration is available for the material parameters.

42   KEYWORDS: landslides, shear strength, temperature effects, strain localization, creep, pore

43   pressures.

44

45   **Notation list**

46   A: model parameter defining the effect of velocity on strength

47   a: model parameter defining the effect of strain rate on friction angle

48   c_s: specific heat of solid particles

49   c_w: specific heat of water

50   D: planar landslide thickness

51   E: energy barrier

52   e: thickness of the shear band

53   E_1:   reference energy barrier

54   f^*:   basic friction for $v=v^*$ and $\psi=0$

55   f_v: function defining the effect of sliding velocity on friction angle

56   g: gravitational acceleration

57    $\hat{H}$:   dimensionless heat generated in the shear band

58   h_w: water height above the sliding plane

59   k: saturated permeability

60   L_{u_w} :   z coordinate where a boundary condition for excess pore water pressure is applied

61   L_θ :   z coordinate where a boundary condition for temperature is applied

62    $\hat{L}_\theta$:   dimensionless L_θ

63   m_{soil}:   compressibility coefficient of the soil skeleton

64 m_v: oedometric compressibility coefficient of soil

65 n: porosity

66 p_w: initial pore water pressure

67 $\hat{p}_w$: dimensionless initial pore water pressure

68 R: universal gas constant

69 SF: safety factor

70 T: absolute temperature

71 t: time

72 u_w: excess pore water pressure

73 $\hat{u}_w$: dimensionless excess pore water pressure

74 $\hat{u}_w^{\max}$: dimensionless maximum excess pore water pressure

75 v^*: velocity below which friction does not depend on velocity

76 v: sliding velocity

77 $\hat{v}$: dimensionless sliding velocity

78 v_1: reference shearing rate

79 v_{ref}: reference velocity

80 $\hat{v}_{ref}$: dimensionless reference velocity

81 z: vertical spatial coordinate

82 $\hat{z}$: dimensionless vertical spatial coordinate

83	α_w:	compressibility coefficient of water
84	β:	inclination of sliding surface
85	β_s:	thermal expansion coefficient of solid particles
86	β_{soil}:	thermal expansion coefficient of saturated porous media
87	β_w:	thermal expansion coefficient of water
88	$\dot{\delta}$:	sliding velocity
89	$\dot{\varepsilon}$:	strain rate
90	$\dot{\varepsilon}_0$:	reference strain rate
91	ϕ'_0:	reference frictional angle associated with a reference strain rate ($\dot{\varepsilon}_0$)
92	ϕ':	effective friction angle
93	γ_w:	water specific weight
94	Γ:	Fourier's thermal conductivity of saturated porous media
95	Γ_s:	Fourier's thermal conductivity of solid particles
96	Γ_w:	Fourier's thermal conductivity of water
97	μ:	friction coefficient
98	μ_0:	reference friction coefficient
99	Θ:	dimensionless coefficient associated with heat flow in the heat balance equation
100	θ:	temperature
101	$\hat{\theta}$:	dimensionless temperature

102 θ_0: reference temperature

103 Π: dimensionless coefficient associated with thermal expansion of porous rock in the

104   mass balance equation of water

105 ρ: density of saturated porous media

106 ρ_s: density of solid particles

107 ρ_w: water density

108 $(\rho c)_s$: specific heat of saturated porous media

109 σ: normal stress to the sliding plane

110 σ_c: normal stress to the sliding plane acting at molecular scale

111 τ: shear stress along the sliding plane

112 τ_c: shear adhesion stress acting at molecular scale

113 Σ: dimensionless coefficient associated with stress induced volumetric deformation in the

114   mass balance equation of water

115 ξ_0: reference value of ξ

116 ξ: state variable which accounts for strengthening and weakening effects on the friction

117   coefficient

118 Ω: active volume of contact bonds

119 Ψ: dimensionless coefficient associated with the source term in the heat balance

120   equation

121     $\bar{\Psi}$:   variable to include other effects than those associated with shearing velocity on

122   frictional strength

123

124   Thermo-poro-mechanical analysis of landslides: from creeping behaviour to catastrophic

125   failure

126   E. E. Alonso, A. Zervos, N.M. Pinyol

127   1. INTRODUCTION

128   Large catastrophic landslides are a constant threat to human communities and infrastructure

129   works. Their danger derives from the large volumes of rock mass they involve (well in excess of

130   1million m^3) and their high estimated sliding velocities (10m/s to 100m/s). Sosio et al (2008)

131   list a number of historical rock avalanches and their main characteristics. The known number

132   of catastrophic landslides is, however, much larger and there is a continuous arrival of new

133   cases, triggered by different natural and anthropogenic causes: earthquakes, heavy rain,

134   reservoir impounding and rapid drawdown and excavations or river erosion. A wider view of

135   catastrophic landslides at a regional scale and its interaction with other geodynamic processes

136   is given by Hewitt et al (2008). Active mountain formation and the associated ongoing crustal

137   plate collisions indicate the natural occurrence of these events, which is not expected to

138   decrease in time.

139   A classic landslide that has been extensively studied is that of Vaiont; Hendron and Patton

140   (1985), Müller (1964), Nonveiller (1987), Semenza (2001) and Paronuzzi et al (2013) provide

141   detailed and informative contributions. Other large scale catastrophic landslides associated

142   with reservoir operations have been reported by Alcántara-Ayala and Domínguez-Morales

143   (2008) (San Juan de Grijalva slide in Mexico, 2007); Wang et al (2004) and Dai et al (2004)

144   (Qiangjianping slide in China, towards the reservoir of the Three Gorges Project, 2003);

145   Chamot (1993), Plaza-Netos and Zevallos (1994), Schuster *et al.,* (2002) and Harden (2004) (La

146   Josefina landslide, Ecuador, in 1993). An often reported case in recent years is the giant

147   Tsaoling landslide, Taiwan, that was triggered by the 1999 Chi-Chi earthquake (Chen et al,

148   2003; Tang et al, 2009; Liao et al, 2011; Wu and Chen, 2011; Yang et al, 2014.) In general, the

149   interpretation of earthquake induced motion requires velocity- and, in some cases,

150   displacement-dependent shear strength weakening of the failure surface. This "slip

151   weakening" effect is discussed below because of its attributed relevance to the sudden

152   acceleration of rapid slides.

153   The morphology and dynamics of these events is quite diverse. Hungr et al (2014) provide an

154   updated classification of landslides but, for the purpose of this paper, we may broadly

155   distinguish flow-like motions from motions with a dominant sliding mode of deformation. This

156   distinction is relevant when considering the mathematical methods of analysis available. In the

157   first case hydrodynamic motion equations and soil/rock properties often associated with the

158   concept of viscosity have been developed (Iverson et al 1997; Cascini et al 2010; Pastor et al

159   2014). In the second case attention is concentrated on the position and frictional

160   characteristics of the sliding surfaces, which should satisfy conditions of kinematic

161   compatibility. This is the approach followed here. Further, a large number of numerical

162   modelling techniques exist, capable of simulating landslide initiation and motion. Methods for

163   the analysis of continua such as the FEM or the MPM (Duncan 1996; Więckowski et al 1999;

164   Darve and Laouafa, 2000; Bardenhagen & Kober 2004; Conte et al 2010; Andersen & Andersen,

165   2010; Pinyol et al 2011; Zabala and Alonso 2011; Yerro et al 2014; Alonso et al 2014) may

166   describe the deforming mass by elastoplastic constitutive equations familiar in Soil Mechanics.

167   DEM and related procedures describe the moving mass by laws of interaction between

168   particles or blocks (Cleary and Campbell 1993; Campbell et al 1995).

169   If the main deformation mechanism considered is one of sliding along localized and thin

170   shearing surfaces, the underlying assumption is that these surfaces are already fully

171   developed. Of the four different types of slope movements described by Leroueil (2001) we

172   are thus concerned with the post-failure stage following first-time failures, which includes the

173   movement of the sliding mass from immediately after the full development of the shearing

174   surface till it comes to rest, and with reactivated slides, where movement restarts along a pre-

175   existing failure surface developed during a past event. It is physical and physicochemical

176   processes occurring at these shearing surfaces that determine the slide's motion and its

177   evolution in time. However, the enormous difference of scale between the thickness of the

178   shearing band and that of the slide raises difficulties. Integration of both scales in a common

179   calculation procedure requires a trade-off, as methods providing a reasonable description of

180   the entire moving mass are ill-conditioned to describe complex physical mechanisms at the

181   scale of a shearing band. However, a combination of simple dynamic equilibrium models for

182   the entire slide and closer attention to the deforming shearing bands proves useful. This is the

183   approach followed here, in line with Voight and Faust (1982), Hendron and Patton (1985),

184   Vardoulakis (2002), Veveakis et al (2007), Pinyol and Alonso (2010a, 2010b), Goren and

185   Aharonov (2009), Cecinato et al (2011), Cecinato and Zervos (2012). In all these cases the heat

186   generated by friction and the resulting pressurization of interstitial water were fundamental

187   parts of the analysis; their relevance in explaining high landslide velocities was first highlighted

188   in the pioneering contributions of Habib (1975); Uriel and Molina (1977) and Voigt and Faust,

189   (1982). Table 1 summarizes the main aspects of published contributions on thermal effects and

190   rapid landslide triggering.

191   The scope of the paper is limited to landslides whose evolving geometry is characterized by soil

192   or rock masses that essentially maintain their original bulk stiffness and strength. The motion is

193   explained by localized shearing surfaces such as those often located in clayey strata described

194   as indurated claystones or overconsolidated clays. Interestingly, Tang et al (2009) observe that,

195   despite the heavy internal fracturing observed in many large landslides, they show a

196   "remarkable tendency to remain in a more or less unchanged sequential order"; this helps

197   extend the analysis described here to a larger class of landslides.

198 From a geotechnical perspective, it is important to distinguish between first-time failures and

199 reactivation of ancient landslides. The first type develops in "intact" sites. They are difficult to

200 analyze, especially when brittle materials are involved in the vicinity of the potential failure

201 surface, as is the case of hard soils or soft argillaceous rocks, in particular those of high

202 plasticity. The strength operating in practice and the geometry of the failure surface are

203 difficult to predict because the failure mechanism develops progressively. Early classic studies

204 on this topic were published by Skempton et al. (1967), Bjerrum (1967) and Bishop (1967,

205 1971). More recent contributions include those by Cooper (1998), Potts *et al.* (1990), Dounias

206 *et al.* (1990), Mesri and Shahien (2003), Gens and Alonso (2006) and Zabala and Alonso (2010).

207 In contrast, re-activated ancient landslides occur on a pre-existing sliding surface that has been

208 subjected to an increasing history of accumulated relative displacements. Hence, it is expected

209 that cohesion will be insignificant on the sliding surface and the friction angle will be close or

210 equal to residual values. It is widely accepted that ancient landslides exhibit a low safety factor

211 close to conditions of strict equilibrium (SF=1). ICOLD (2002) reports that in at least 75% of

212 cases where old landslides (active or inactive) are disturbed, e.g. by an excavation or by

213 submerging the toe, slide reactivation or an increase in velocity is observed. It is also

214 frequently observed, especially in consolidated clayey strata, that a very low value of friction

215 angle, even lower than the residual friction determined in ring shearing tests, operates in

216 joints and shearing zones of ancient landslides. The evolution of residual strength during

217 resting times is a controversial subject which has been discussed in Alonso and Pinyol (2014).

218 Consider, as an introduction to the remainder of the paper, the motion of a block sliding on a

219 friction-resistant surface inclined at angle β. Velocity increases linearly with time, *t*, following

220 the equation:

221 $v = g \sin \beta \left(1 - SF \right) t$ (1)

222   where g is the gravity acceleration and SF the initial safety factor, defined as the ratio between

223   resisting (shear strength) and disturbing shear stress. If SF=1.0 the block remains still. To

224   initiate motion it is necessary to introduce some imbalance between resisting and disturbing

225   stress. In real situations involving re-activated slides the imbalance may have different origins

226   but it is typically small; e.g. raising the water level in a reservoir slowly affects pore pressures

227   in the valley upstream.

228   For SF=0.99 and β=10º, equation (1) predicts that a catastrophic sliding velocity of 1m/s will be

229   reached in 58s. However field evidence does not support this result. A reasonable explanation

230   is that the friction angle increases slightly as slide motion causes the rate of shearing on the

231   failure plane to increase. Then SF increases to SF=1 and the slide reaches dynamic equilibrium

232   and exhibits creeping motion, i.e. it moves with constant or near-constant velocity that is also

233   relatively low.

234   Experience also indicates (this is the case of Vaiont) that a relatively slow creep motion of a

235   few mm/day may evolve to 30m/s in 15s. However equation (1) predicts, for the same slope

236   angle, that for a small reduction of SF by 1% it takes 30 minutes to reach 30m/s. Therefore

237   equation (1) is unable to explain observations at the two scales of the motion of interest in

238   practice: the creeping states and the eventual catastrophic outcome.

239   Material brittleness may explain a significant reduction of shear strength at the start of the

240   motion. It may be invoked in cases of first time failures but it cannot be easily justified in re-

241   activated slides or in creeping motions that may evolve into a rapid slide. It may be also

242   present in compound sliding motions which require shearing across "intact" rock and not only

243   on the basal sliding surface. This is certainly an acceptable scenario in some cases but it cannot

244   explain the rapid motion of planar slides, which is a common case.

245   This paper is organized as follows: The question of the strain rate dependence of friction is

246   discussed in Section 2. In Section 3 a thermo-poro-mechanical model for an infinite planar slide

247   is presented, using appropriate dimensionless variables. Section 4 discusses the numerical

248   methods developed to solve the corresponding initial/boundary value problem, and Section 5

249   contains a range of numerical results that provide insights into the underlying phenomena.

250   Some conclusions are presented in Section 6.

251

252   2. STRAIN RATE DEPENDENT FRICTION AND PRECURSORY SLIDING MOTIONS

253   Before discussing some results of shearing experiments it is convenient to briefly examine

254   some basic concepts of the theoretical understanding of friction. The initial contributions are

255   presented in Bowden & Tabor (1964). Mitchell (1976) and Rice (2001) describe how employing

256   the theory of "activation energy" at the level of microscopic contacts leads to the common law

257   of friction. A frictional contact is idealised as a number of isolated contact points (Fig. 1) where

258   adhesion (τ_c) and normal stresses (σ_c) are understood to act at the scale of molecular

259   interactions between the minerals in contact. Normal and shear stresses are expected to reach

260   high local values and are controlled by chemical reactions. Using equilibrium, the macroscopic

261   shear and normal stresses (τ and σ) are related to their microscopic counterparts as:

262    $$\tau = \sigma \frac{\tau_c}{\sigma_c} \tag{2}$$

263

       which justifies why shear stress is linearly related to normal stress.

264   However, under transient shearing, chemical reactions at the molecular scale of the isolated

265   process zones of the local contacts are expected to change the value of the adhesion stresses

266   (τ_c). If local chemical reactions follow a rate process, their velocity of reaction can be written:

267    $$v = v_1 \exp\left(-\frac{E}{RT}\right) \tag{3}$$

268   where E is the activation energy, T is absolute temperature, R is the gas constant and v_1 is a

269   reference shearing rate. The interpretation of this equation is that the energy E in equation (3)

270   allows a shearing rate velocity v. E has the meaning of a threshold energy barrier: if it

271   decreases, velocity increases. Applied stresses decrease the energy barrier and increase the

272   velocity of the processes taking place at the point contacts and, therefore, the velocity of

273   deformation. Stress is understood as energy per unit volume, so the effect of stress on the

274   energy barrier E can be expressed as:

275   $$E = E_1 - \tau_c \Omega \tag{4}$$

276   where Ω is an active volume of contact bonds and E_1 is a reference energy barrier. Equations

277   (3) and (4) lead to

278   $$\tau = \sigma \left[\frac{E_1}{\Omega \sigma_c} + \frac{RT}{\Omega \sigma_c} \ln \frac{v}{v_1} \right] \tag{5}$$

279   which predicts a linear increase of friction with the logarithm of shearing velocity. The

280   reference term $E_1/(\Omega \sigma_c)$ is interpreted as a basic friction which may depend on the state of the

281   frictional surface; "state" may include shearing relative displacement, applied stress and time

282   (Rice et al, 2001). The friction law may then be written,

283   $$\frac{\tau}{\sigma} = f = f^* + \bar{\psi} + A \ln \frac{v}{v^*} \tag{6}$$

284
285   where f^* is a basic friction and $\bar{\psi}$ includes effects other than those associated with shearing

286   velocity.

287   Experimental results at low shearing rates tend to support equation (6). For instance, based on

288   direct and ring shear tests of highly plastic clay layers of the Clearwater formation in Alberta,

289   Canada, Wedage et al. (1998) proposes the following empirical relationship between residual

290   friction and shearing rate:

291 $$\tan\phi = \tan\phi_0 \left(1 + a\,\ln\frac{\dot{\varepsilon}}{\dot{\varepsilon}_0}\right)$$ (7)

292   Cooper et al (1999) investigated the effect of rate of shear on ring shear tests performed on

293   high plasticity Gault clay. Shearing rates varied almost four orders of magnitude, from 0.5

294   mm/min to 0.0001 mm/min, but still within the range expected in creeping slide motions. Tika

295   et al (1996) extended the rate of shearing to the range 10^{-5} to 10^{4} mm/min and concluded that

296   the evolution of residual strength depends on the type of soil. They found that some soils

297   exhibit a "negative" rate effect of the residual strength, which was explained as result of an

298   increase in water content in the shear zone, because of the dilatant effect of "turbulent"

299   shearing (which requires some granular content). Skempton (1985) presented results of ring

300   shear test on clays conducted at rates from 100 times faster to 100 times slower than the

301   commonly used 0.01mm/min; they show that the residual strength increased by about 2.5%

302   per log cycle increase in strain rate, an increase that Skempton (1985) acknowledges can cause

303   large changes in the rate of movement.

304   Direct shear tests on polished surfaces of rock (Dieterich, 1979, Ruina, 1983) support a linear

305   increase of the friction coefficient with the logarithm of the shearing rate. Alternative

306   proposals have also been presented, e.g. Davis *et al*. (1993) propose:

307 $$\frac{\tau}{\sigma} = f = f^* + b\frac{v}{v_r}\exp\left(\frac{-v}{v_r}\right)$$ (8)

308   The velocity term in Equation (8) provides an initial increase in friction with velocity followed

309   by a decrease for $v > v_r$.

310   Testing devices capable of shearing soil samples to velocities in excess of 0.1 m/s have been

311   developed in the past decade. Temperature in these tests rises to values that can cause

312   transformation of minerals. As a rough guide, montmorillonite loses water molecules from

313   interlayers at temperatures <200 ºC; kaolinite loses water and transforms into a complex

314   amorphous structure of aluminum and silica compounds at about 550ºC and calcite transforms

315   into CaO and releases CO_2 gas at temperatures of 600ºC - 850ºC.

316   Ujiie and Tsutsumi (2010) report the results of tests performed on clayey gouges in a rotary

317   shear apparatus capable of measuring the shearband temperature. In saturated samples,

318   temperature increase and reduction of apparent friction under high shearing velocity (in

319   excess of 0.1mm/s) develop in tandem. The authors attributed the loss of friction to the

320   thermally induced dilation of water and concluded that mineral de-hydration and water

321   vaporization were not responsible for the rapid "slip weakening" observed. For shearing rates

322   below 0.1 mm/s it was found that the clay gouge exhibited friction strengthening; this is

323   consistent with data reported by Tika et al (1996).

324   Many authors have reported in recent years the results of high velocity shearing (limited to

325   around 1.3m/s in most cases) in a variety of soil types (Di Toro et al, 2006; Mizoguchi et al,

326   2007; Ferri et al, 2010; Liao et al 2011; Han and Hirose, 2012; Yang et al, 2014) tested both

327   saturated and unsaturated. The soils tested are typically a mixture of quartz, carbonate

328   minerals and clay minerals. Pore pressures and temperatures were, apparently, never

329   measured. These tests as well as field observations (e.g. the presence of sheared mud in joints

330   adjacent to the main shearing surface; the observation of molten rock injected from the sliding

331   surface into the fault after earthquakes) indicate that the shearing strength reduction may

332   have the following origins: grinding of minerals into nanoparticles of low friction; de-hydration

333   of minerals and the associated increase in pore pressure; de-carbonation of calcite and the

334   release of pressurized gas; melting of minerals, resulting in a viscous material and thermal

335   pressurization because of the different dilation coefficients of water and minerals, in the case

336   of saturated soils. Lack of saturation enhances the transformation of clay minerals and the

337   release of CO_2, which is an indication of unsaturated samples attaining higher temperatures

338   compared with saturated ones. The results can be explained by considering that saturation

339   allows the reduction of normal effective stress to very small values, in turn reducing heat

340   production despite the high shearing rate. This is consistent with the results of Ujiie and

341   Tsutsumi (2010) mentioned above.

342   Shearing rates in creeping slides are not expected to exceed 0.1-1 mm/s in practice. Therefore

343   the notion of creeping can be explained by friction strengthening with increasing shearing rate,

344   without the need to invoke the concept of viscosity. On the other hand, the extension of

345   friction-rate relationships such as equations (6), (7) or (8) to high shearing rates is more

346   uncertain.

347   The question of the transformation of a creep motion into an accelerated motion eventually

348   leading to failure has also been approached from a different perspective. Monitoring of slope

349   deformations suggests that the time to failure may be predicted by relating linearly the inverse

350   of velocity with time (Saito, 1965, 1969; Voight, 1978). Helmstetter et al (2003) discuss the

351   rationale behind these procedures. They further examine the effect of friction strain rate and

352   state dependence by considering the dynamics of a simple sliding block in conjunction with the

353   friction law given by equation (6), elaborated as:

354    $$\mu = \mu_0 + A \ln \frac{\dot{\delta}}{\dot{\delta}_0} + B \ln \frac{\xi}{\xi_0}$$ (9)

355   where μ is the friction coefficient, $\dot{\delta}$ is the sliding velocity, ξ a state variable, subscript 0 refers

356   to reference values and A and B are model parameters. The evolution of the state variable is

357   given by:

358    $$\frac{d\xi}{dt} = 1 - \frac{\xi \dot{\delta}}{D_c}$$ (10)

359   where D_c is interpreted as a critical size of asperities of the shearing surface. Variable ξ may

360   model strengthening actions (aging, for instance) or weakening effects for accumulated shear

361   displacements. The authors concluded that the stability of the motion is controlled by the ratio

362   B/A: $B/A > 1$ leads to instability, where the slope velocity increases continuously. They suggest

363   that this was the case of Vaiont. If 0 < *B/A* < 1 the motion remains stable and the velocity may

364   increase or decrease towards a constant value. They suggest that this is the case of La Clapière

365   (Follacci et al, 1993). The result is very attractive because it seems to provide a simple and

366   elegant solution to a complex problem. However, this model is unable to explain the fast

367   acceleration of the landslide once it has initiated, i.e. the transition from pre-failure velocities

368   of the order of 4cm/day to a final velocity of 30m/sec in an estimated time of 15s. It is

369   concluded that a different physical phenomenon should be explored if such acceleration is to

370   be captured. The situation is sketched in Figure 2. The rate and state dependent laws of

371   friction seem to be capable of predicting creeping behaviour and even a (slow) transition

372   towards failure (a phenomenon also known as tertiary creep). But they are not capable of

373   explaining very fast slide accelerations starting at a state of creeping velocities. Modelling this

374   transition is the subject of the next section.

375   In the remaining of this paper the following rate dependent friction angle will be used:

376    $$\tan \phi = \tan \phi_0 \left(1 + A \ln \frac{v}{v_0} \right) \qquad\qquad (10)$$

377   where v is the sliding velocity across the shear band and v_0 is a reference velocity.

378   Interpretation of the reported results on residual friction of clayey soils indicates that the rate

379   parameter A can be taken to vary between extremes of 10^{-5} and 10^{-2}. For a baseline friction

380   of $12°$ and a reference velocity $v_0 = 0.01 mm/min$, this range implies that a four-orders-of-

381   magnitude increase of velocity will lead to an increase in the residual friction angle between

382    $0.01°$ for $A = 10^{-5}$, which is negligible, and $5.7°$ for $A = 10^{-2}$, which represents an extreme,

383   near-50% increase over the baseline value.

3. A THM STRAIN RATE DEPENDENT SLIDING BLOCK MODEL. PROBLEM FORMULATION

Problem Description

Consider a slope inclined an angle β and a planar landslide with constant thickness D (Fig. 3). The sliding mass moves as a rigid body and deformations concentrate in a shear band of thickness 2*e* parallel to the slope surface (Fig.3). The shearing zone is a large planar surface compared with the band thickness, undergoing uniform deformation. A linear profile of shearing velocity inside the band is assumed. Temperature and pore pressure build-up will be concentrated into the shear band and its vicinity. Therefore the analysis may be formulated as one-dimensional in the direction normal to the band. Water and energy transfer become one-dimensional processes along the spatial coordinate *z* (Fig.3). The band thickness is typically small, in the range of a few mm or cm. Shear bands in real cases are often embedded in thicker layers of claystone or clay bearing rocks, whose properties the band material may be assumed to share.

Water flow parallel to the slope, over height h_w above the sliding plane, is assumed (Fig. 3).

Dimensionless Governing Equations

The landslide motion is described using the dynamics equation. Acceleration results from the difference between gravitational driving forces and frictional resistance forces along the shear band. Frictional forces are controlled by the pore water pressure which is equal to the sum of the initial pore water pressure, present before movement initiates, and any excess pore water pressure generated during sliding due to shearing induced heating. Pore pressure and heat dissipation occur simultaneously and are governed by the corresponding mass and energy balance equations inside and outside the shear band.

The following dimensionless variables have been selected to write the governing equations:

408 $\hat{z} = \dfrac{z}{D}$, $\hat{t} = \dfrac{t\sqrt{gD}}{D}$, $\hat{\theta}(\hat{z},\hat{t}) = \dfrac{\theta(z,t)}{\theta_0}$, $\hat{u}_w(\hat{z},\hat{t}) = \dfrac{u_w(z,t)}{\rho gD}$, $\hat{p}_w = \dfrac{p_w}{\rho gD}$, $\hat{v}(\hat{t}) = \dfrac{v(t)}{\sqrt{gD}}$ (11)

409 where t is the time, θ the temperature, u_w the excess pore water pressure, p_w the initial pore

410 water pressure and v the landslide velocity. $\rho = n\rho_w + (1-n)\rho_s$ is the density of the

411 saturated soil, expressed in terms of porosity, n, and the densities of water ρ_w and solid

412 particles ρ_s. g is the gravitational acceleration and θ_0 is a reference initial temperature,

413 assumed equal to 10ºC in the calculations reported below. The governing equations and initial

414 and boundary conditions of the problem are expressed as follows:

415 *Dynamic equilibrium*:

416 $\dfrac{d\hat{v}(\hat{t})}{d\hat{t}} = \sin(\beta) - \left(\cos(\beta) - \dfrac{\hat{p}_{wh}}{\cos(\beta)} - \dfrac{\hat{u}_w^{\max}(\hat{t})}{\cos(\beta)} \right) \tan\varphi'$ (12)

417 Initial condition: $\hat{v}(\hat{t}=0) = 0$

418 *Energy balance equation*:

419 $\dfrac{\partial\hat{\theta}(\hat{z},\hat{t})}{\partial\hat{t}} - \dfrac{\Gamma}{(\rho c)_m D\sqrt{gD}} \dfrac{\partial^2\hat{\theta}(\hat{z},\hat{t})}{\partial\hat{z}^2} = \hat{H}(\hat{z},\hat{t})$ (13)

420 where

421 $\hat{H}(\hat{z},\hat{t}) = \dfrac{\rho gD^2}{(\rho c)_m \theta_0 2e} \left(\cos^2(\beta) - \hat{p}_{wh} - \hat{u}_w^{\max}(\hat{t}) \right) \tan\varphi' \hat{v}(\hat{t})$ for $\hat{z} \in [0, e/D]$ (14a)

422 $\hat{H}(\hat{z},\hat{t}) = 0$ for $\hat{z} \in (e/D, L_\theta]$ (14b)

423

424

425

426

427   Initial and boundary conditions are given by:

$$
\begin{cases}
\hat{\theta}\left(\hat{z},\hat{t}=0\right)=1 & \text{(15a)} \\[2mm]
\left.\dfrac{\partial\hat{\theta}}{\partial\hat{z}}\right|_{\left(\hat{z}=0,\hat{t}\right)}=0 & \text{(15b)} \\[2mm]
\hat{\theta}\left(\hat{z}=e^{-}/D,\hat{t}\right)=\hat{\theta}\left(\hat{z}=e^{+}/D,\hat{t}\right) & \text{(15c)} \\[2mm]
\left.\dfrac{\partial\hat{\theta}}{\partial\hat{z}}\right|_{\left(\hat{z}=e^{-}/D,\hat{t}\right)}=\left.\dfrac{\partial\hat{\theta}}{\partial\hat{z}}\right|_{\left(\hat{z}=e^{+}/D,\hat{t}\right)} & \text{(15d)} \\[2mm]
\hat{\theta}\left(\hat{z}=L_{\theta}/D,\hat{t}\right)=1 & \text{(15e)}
\end{cases}
$$

428   The specific heat of the saturated porous medium is calculated using a weighted average:

429    $\left(\rho c\right)_{m}=n\rho_{w}c_{w}+\left(1-n\right)\rho_{s}c_{s}$ where c_{w} and c_{s} is the specific heat of water and solid particles

430   respectively. Fourier's thermal conductivity is also calculated as a weighted average

431    $\Gamma=n\Gamma_{w}+\left(1-n\right)\Gamma_{s}$, where Γ_{w} and Γ_{s} the conductivity of water and solid respectively. In line

432   with (Alonso and Pinyol, 2010b), advective heat transfer is neglected.

433   The dimensionless source term $\hat{H}\left(\hat{t}\right)$ in equation 14a quantifies the heat input into the shear

434   band in terms of the work consumed per unit volume of the material by its shear strength.

435   Outside the band, where the mass moves as a rigid body, no heat is generated (eq. 14b).

436   Regarding initial and boundary conditions, the first condition (eq. 15a) imposes that initially

437   the shear band and surrounding zone are at the reference temperature. No heat is transferred

438   across the center of the shear band and therefore no heat flow is imposed at $\hat{z}$ =0 (eq. 15b).

439   Continuity of temperature and temperature flow should be satisfied on both sides of the shear

440   band (eq. 15c and 15d). The temperature boundary condition at $\hat{z}=L_{\theta}/D$ (eq. 15e) stipulates

441   that temperature remains unaffected beyond a pre-determined distance L_{θ} from the axis of

442   the shear band. If taken further away from the shear band than heat flow will reach during the

443   time frame modelled, L_{θ} does not affect the results.

444   *Mass balance equation:*

445
$$-\frac{\beta_{soil}\theta_0}{m_{soil}\rho g D}\frac{d\hat{\theta}(\hat{z},\hat{t})}{d\hat{t}}+\frac{d\hat{u}_w(\hat{z},\hat{t})}{d\hat{t}}-\frac{k}{\gamma_w m_{soil}D\sqrt{gD}}\frac{d^2\hat{u}_w(\hat{z},\hat{t})}{d\hat{z}^2}=0 \qquad (16)$$

446 Initial and boundary conditions are given by:

$$\hat{u}_w(\hat{z},\hat{t}=0)=0 \qquad (17a)$$

$$\left.\frac{\partial \hat{u}_w}{\partial z}\right|_{(\hat{z}=0,\hat{t})}=0 \qquad (17b)$$

$$\hat{u}_w(\hat{z}=e^-/D,\hat{t})=\hat{u}_w(\hat{z}=e^+/D,\hat{t}) \qquad (17c)$$

$$\left.\frac{\partial \hat{u}_w}{\partial z}\right|_{(\hat{z}=e^-/D,\hat{t})}=\left.\frac{\partial \hat{u}_w}{\partial z}\right|_{(\hat{z}=e^-/D,\hat{t})} \qquad (17d)$$

$$\hat{u}_w(\hat{z}=L_{u_w}/D,\hat{t})=0 \qquad (17e)$$

448 In the mass balance equation (16), β_{soil} is a weighted average thermal expansion coefficient for

449 saturated soils calculated as: $\beta_{soil}=n\beta_w+(1-n)\beta_s$, where β_w and β_s are the thermal expansion

450 coefficients of water and solid particles respectively. These depend on temperature, e.g.

451 Wagner and Kruse (1998); however as a first approximation they are assumed here to be

452 constant. m_{soil} is the compressibility of saturated soil, calculated as $m_{soil}=m_v+n\alpha_w$ where m_v

453 and α_w are the coefficients of compressibility of the soil skeleton and the water respectively.

454 k is the saturated permeability of the soil.

455 Initial and boundary conditions are similar to those imposed for heat transfer. The initial value

456 of excess pore pressure is zero (eq. 17a). No water flow crosses the center of the shear band

457 (eq. 17b). Equations 17c and 17d ensure continuity of excess pore pressure and flow rate on

458 both sides of the band. The excess pore pressure is assumed zero beyond a pre-determined

459 distance L_{u_w}. If this distance is far enough for excess pore pressure to not develop there, it

460 does not affect the results; otherwise it stipulates the existence of a drainage boundary.

461   L_θ and/or L_{u_w} may be interpreted as the thickness of the claystone layer containing the shear

462   band: pore pressure and temperature should be maintained constant at its outer boundary.

463   Alternatively, if the layer is in contact with a pervious rock mass, it is reasonable for these

464   conditions to apply at the interface.

465   Four dimensionless coefficients are naturally defined in the balance and equilibrium equations.

466   They are associated with the physical phenomena describing the problem:

467    $\Theta = \dfrac{\Gamma}{(\rho c)_m D \sqrt{gD}}$, coefficient associated with heat flow in the heat balance equation;

468    $\Psi = \dfrac{\rho g D^2}{(\rho c)_m \theta_0 2e} = \dfrac{\rho D (\sqrt{gD})^2}{(\rho c)_m \theta_0 2e}$, coefficient of the source term in the heat balance equation;

469    $\Pi = \dfrac{\beta_{soil}}{m_{soil}} \dfrac{\theta_0}{\rho g D}$, coefficient associated with thermal expansion of porous rock in the mass

470   balance equation of water;

471    $\Sigma = \dfrac{k}{\gamma_w m_{soil} D \sqrt{gD}}$, coefficient associated with stress induced volumetric deformation in the

472   mass balance equation of water;

473   Θ is a measure of the thermal dissipation and combines thermal conduction, heat storage, a

474   reference dimension and a reference velocity; Ψ can be interpreted as the ratio between the

475   kinetic energy of the moving mass and the initial heat stored in the shear band, Π is a ratio of

476   the thermal expansion of the saturated porous medium with respect to its mechanical

477   compressibility and Σ is a dimensionless consolidation coefficient that combines permeability,

478   confined compressibility and the sliding depth.

479   For a given planar landslide of thickness D, the range of variation of the non-dimensional

480   parameters is limited. Properties such as density, Fourier's coefficient, thermal expansion

481   coefficient and the specific heat for common soils and rocks exhibit small variation especially if

482   compared with other parameters such as permeability. Typical values for these material

483   properties are indicated in **Error! Reference source not found.**. On the contrary, permeability,

484   k, soil compressibility, m_v, and thickness of the shear band, e, may change more significantly.

485   Typical ranges of values of these variables are collected in **Error! Reference source not found.**.

486   As a consequence, the dimensionless parameters that may vary significantly depending on the

487   particular case analyzed are: Ψ which is inversely proportional to the band thickness; Π

488   which is inversely proportional to the band compressibility coefficient; and Σ which depends

489   on the ratio of permeability and soil compressibility.

490   Using **Error! Reference source not found.** and **Error! Reference source not found.**, ranges for

491   the values of the non-dimensional parameters can be established. Θ is essentially constant

492   and equal to $1.27 \cdot 10^{-9}$. Ψ depends on the shear band thickness and may vary between 30 and

493   1800. Π may vary by two orders of magnitude, roughly between 0.1 and 10, due to the

494   variability of the shear band compressibility coefficient. Finally, Σ depends on the ratio

495   between permeability and compressibility so its range of variation is much wider, between 10^{-3}

496   and 10^{7}. Shear bands are often located in highly overconsolidated layers having a wide range

497   of clay mineral content. Their compressibility will be closer to the medium and low values

498   within the range indicated in Table 2, reducing the variability mainly of Π but also of Σ in

499   practice. Permeability remains as the main source of variability.

500   *Zero thickness shear band*

501   Idealizing the sliding surface as a zero thickness shearing band may be sufficiently close to

502   actual conditions, especially in highly plastic materials where sliding surfaces are often

503   described as smooth and polished planes. In terms of problem formulation and its numerical

504   solution, the hypothesis of zero band thickness presents some advantages: a) the geometry is

505   simplified and one of the parameters entering the dimensionless formulation, the band

506   thickness, 2*e*, disappears and b) the discretization of the domain is simplified because there is

507   no need to discretize the very thin band.

508   The rate of frictional work expended along the contact plane, per unit of surface, is now

509   calculated as the product between shear strength and velocity. This mechanical work

510   dissipates into heat that enters the rock mass. With reference to Figure 1, when 2*e*=0, the

511   coordinate *z*=0 indicates the position of the contact plane.

512   The system of equations governing the problem is similar to the system for finite band

513   thickness. The difference lies in the heat balance equation, which becomes:

514
$$\frac{\partial \hat{\theta}\left(\hat{z},\hat{t}\right)}{\partial \hat{t}} - \frac{\Gamma}{\left(\rho c\right)_m D\sqrt{gD}} \frac{\partial^2 \hat{\theta}\left(\hat{z},\hat{t}\right)}{\partial \hat{z}^2} = 0$$

515   with the following initial and boundary conditions:

$$\begin{cases} \hat{\theta}\left(\hat{z},\hat{t}=0\right)=1 \\[2mm] \left.\dfrac{\partial \hat{\theta}}{\partial \hat{z}}\right|_{\left(\hat{z},\hat{t}=0\right)} = 0 \\[4mm] \dfrac{1}{2}H\left(\hat{t}\right) = -\dfrac{\Gamma\theta_0}{D}\left.\dfrac{\partial \hat{\theta}}{\partial \hat{z}}\right|_{\left(\hat{z}=0,\hat{t}\right)} \Rightarrow \left.\dfrac{\partial \hat{\theta}}{\partial \hat{z}}\right|_{\left(\hat{z}=0,\hat{t}\right)} = -\dfrac{\rho g D^2 \sqrt{gD}}{2\Gamma\theta_0}\left(\cos^2\left(\beta\right)-\hat{p}_{wh}-\hat{u}_w^{\max}\left(\hat{t}\right)\right)\tan\varphi'\hat{v}\left(\hat{t}\right) \\[4mm] \hat{\theta}\left(\hat{z}=L_0/D,\hat{t}\right)=1 \end{cases}$$

516   Note that no heat is generated in the sliding mass, but heat flow is imposed through a

517   boundary flux at $z=0$. Because of symmetry only half of the heat generated is considered.

518   The dimensionless parameters describing this problem remain identical to the case of finite

519   band thickness except for the coefficient associated with the source term in the heat balance

520   equation, which becomes $\Psi = \dfrac{\rho g D^2 \sqrt{gD}}{2\Gamma\theta_0}$. The heat generated at the boundary is now

521   calculated as:

522
$$H\left(\hat{t}\right) = \rho g D\sqrt{gD}\left(\cos^2\left(\beta\right)-\hat{p}_{wh}-\hat{u}_w^{\max}\left(\hat{t}\right)\right)\tan\varphi'\hat{v}\left(\hat{t}\right)$$

523   *Rate effects*

524   Slow maintained slide displacement rates (creeping) will be explained by considering strain

525   rate effects on strength, following the discussion in Section 2. The analysis concentrates on

526   active slides irrespective of their initial creeping rate; therefore frictional strength is

527   characterized by a residual friction angle. The effective residual friction strength is defined as

528   the sum of the strength available at velocities lower than a given value of reference (v_{ref}) and

529   an additional term that depends on sliding velocity:

530   $$\tan\phi = \tan\phi_0 + f_v \qquad (18)$$

531   Recalling the logarithmic law of Equation (10):

532   $$f_v = A\ln\left(\frac{v}{v_{ref}}\right) = A\ln\left(\hat{v}\frac{\sqrt{gD}}{v_{ref}}\right) \text{ for } v > v_{ref}; \hat{v} > \hat{v}_{ref} = v_{ref}/\sqrt{gD} \qquad (19a)$$

533   $$f_v = 0 \text{ for } v \le v_{ref}; \hat{v} \le \hat{v}_{ref} = v_{ref}/\sqrt{gD} \qquad (19b)$$

534   The slope angle β and the parameters defining the friction law (φ_0', A, $v_{ref}/\sqrt{gD}$) complete the

535   set of dimensionless parameters governing the problem.

536   ## 4. NUMERICAL INTEGRATION

537   Equations (12), (13) and (16) form a system of coupled, non-linear partial differential equations

538   that needs to be solved. The use of centred-space forward-time (explicit) finite differences has

539   been the norm in past work (e.g. Vardoulakis, 2002, Alonso et al, 2010, Cecinato et. al. 2011,

540   2012). However explicit integration requires very small timesteps, typically of the order of

541   10^{-5}sec, for numerical stability. Although acceptable when modelling the catastrophic phase of

542   a slide over its final few tens of seconds, this onerous condition makes modelling of the long-

543   term creep behaviour that may precede failure impractical. The alternative we explore here is

544   the use of an unconditionally stable implicit scheme that will allow much larger timesteps. The

545   ability to adapt the timestep during the calculation is also essential, so that long periods of

546   creep where the solution changes by very little can be modelled efficiently. We use here the

547   trapezoidal rule, which is of order $O(\Delta t^2)$. In principle it is also possible to use a higher order,

548   more accurate multistep method; however adaptive time stepping will only be possible at the

549   cost of significantly increased complexity, e.g. Skeel (1986).

550   The resulting system of equations must be solved iteratively to calculate at the end of each

551   timestep the slide velocity as well as the temperature and excess pore pressure everywhere in

552   the domain. Solution using a full Newton-Raphson method is however problematic, as the

553   logarithmic friction law renders the dynamics equation highly nonlinear. Convergence requires

554   timesteps typically smaller than 10^{-3}sec, defeating the purpose of the implicit scheme.

555   The strategy adopted was to use a staggered solution scheme: the diffusion equations were

556   solved by Newton-Raphson using the current approximation of the velocity; the dynamics

557   equation was subsequently solved by Pegasus (Dowell and Jarratt, 1972), a method of the

558   *regula falsi* family that is known to be fast and efficient in finding roots of nonlinear equations.

559   Iterations continued till the residuals of all equations were below tolerance. The timestep was

560   increased or decreased based on the rate, or lack of, convergence. The maximum timestep

561   used was 24h. This approach allowed timesteps of the order of 10^5sec for the most part of an

562   analysis, making the efficient modelling of years of creeping motion possible.

563   An additional challenge was the location of the far boundary L_θ and L_{u_w}. Previous work

564   considered that ambient values of temperature and excess pore pressure are applicable at a

565   distance equal to a small multiple of the shearband thickness. Although this is valid for rapid

566   heat generation during the final collapse, modelling the creep phase should require a larger

567   domain, as heat and pore water will potentially have the time to travel longer distances. In

568   practice, the presence of a geological feature, such as an interface with pervious rock, may

569   provide a natural boundary within the sliding mass, as discussed previously. For the general

570   case, however, the following numerical approach was adopted: The far boundary was initially

571   considered at a distance 10 times the shearband thickness. If, during the calculation, the value

572   of either the temperature or the excess pore pressure next to the boundary was found to

573   differ by more than 10^{-10} ^{0}C or kPa respectively from the corresponding boundary condition,

574   the domain was expanded by 100 times the shearband thickness before the calculation

575   continued. Therefore the problem progressively became computationally more expensive;

576   typical calculations started with about 300 unknowns but eventually involved in excess of

577   300,000. Nevertheless, due to the direct, sparse multi-frontal solver (HSL, 2015) used, all

578   models could run on a desktop computer within hours.

579   ## 5. ANALYSIS

580   ### 5.1 An illustrative example

581   The case presented below illustrates the capability of the model to integrate a history of

582   creeping motions and the eventual triggering of a rapid catastrophic motion. Basic parameters

583   are given in Table 1. The sliding mass is defined by D=25m, h_{w0} =11.05m, β=9.8º, ϕ_0=12º,

584   $2e$=2.5mm, m_v=1.5.10^{-9}Pa^{-1} and k=10^{-9}m/s . The strain rate effect is characterized by A=0.014

585   and v_{ref} =10^{-5}m/s. An initial temperature θ_0 =10ºC is assumed. The shear band is centered in a

586   clayey layer 2m thick, bounded by pervious rock that is able to maintain the initial pore

587   pressure and temperature.

588   The slope is initially in strict equilibrium with zero velocity. It is destabilized by increasing the

589   water level to h_w=12m. The subsequent history of water level changes is given in Figure 4a.

590   There is a transient reduction of h_w from 13m to 12.5m and a final increase to 14m. During this

591   final stage the slide suddenly accelerates. Figure 4 provides the calculated evolution of

592   temperature (Fig 4b,c), excess pore water pressure (Fig 4d), velocity (Fig 4e), displacement (Fig

593   4f) and friction angle (Fig 4g). Temperature and excess pore pressure increase in the shear

594   band as soon as the slide becomes unstable. The sliding velocity slowly increases; however

595   strain rate effects contribute to maintaining dynamic equilibrium. The subsequent reduction of

596   water level reduces the sliding velocity and the shear band excess pore pressure and

597   temperature. Similar changes occur to the friction angle, Fig. 4g, because of strain rate effects.

598   It can be considered that the slope maintains a safety factor SF=1 during the entire creeping

599   period.

600   When a further increase of water level to h_w=14 m is imposed at t=15000s, temperature and

601   pore water pressure increase rapidly and strain rate effects are no longer capable of

602   maintaining a state of slow creeping velocity. The slide accelerates because the pore pressure

603   reaches values close to the normal effective stress on the sliding surface, rapidly reducing the

604   frictional resistance there.

605   Thermal pressurization affects the behaviour of the slide throughout. However there is a

606   qualitative change when friction increase, induced by rate effects, is no longer capable of

607   counteracting the strength reduction caused by pore pressure build-up in the shear band. At

608   that time the creeping stage ends and the slope enters a high acceleration and high velocity

609   stage promoted by a thermally-dominated "feedback loop": temperature increase-pore

610   pressure increase-strength reduction-velocity increase-temperature increase. From that point

611   onwards strain rate effects no longer play a significant role in the evolution of the slide.

612   The remainder of this chapter explores the relationship between these two regimes of slope

613   behaviour. They are intimately linked and particular cases characterized by a sliding geometry

614   and material properties would require a specific analysis. However, the simple planar slide

615   offers insights on the creep-fast sliding coupling. The dimensionless formulation also enhances

616   the generality of the conclusions reached.

617   5.2 Velocity regimes in a planar slide

618   Results will be presented for a fixed displacement equal to twice the height of the sliding mass.

619   This is an arbitrary limit, however analyses of longer runouts are unlikely to be representative

620   due to topographical constraints and/or the resulting fragmentation of the sliding mass.

621   <u>Rate independent friction</u>

622   We consider again the previous example, this time with rate independent frictional strength.

623   No creeping stage is now possible. This case serves as a reference for the rate dependent case.

624   The landslide is destabilized by imposing an increment of the dimensionless pore water

625   pressure ($\hat{p}_{wh}$) equal to 0.0016, equivalent to increase the water level in 10 cm. It involves a

626   reduction of the SF from SF=1 to SF= 0.9978.

627   The effect of the shear band thickness is first examined. This parameter only affects Ψ, the

628   dimensionless coefficient of the source term in the energy balance equation. **Error! Reference**

629   **source not found.** shows the maximum dimensionless velocity for different values of Ψ and Σ

630   and a constant $\Pi=1$ value. Since Π remains constant for all the cases analyzed, variation of Σ

631   implies essentially variation of the permeability. The two plots in Figure 5 present the same

632   information in two different ways. The nearly horizontal lines in Figure 5a indicate that the

633   effect of parameter Ψ on the velocity reached is small. This is also apparent from Figure 5b,

634   where the calculated velocities for different band thicknesses essentially overlap. Parameter Ψ

635   directly affects the heat generated in the shear band. The higher its value, i.e. the smaller the

636   band thickness, the larger the quantity of heat generated. However, smaller band thickness

637   also means easier dissipation of the heat and excess pore pressure generated within the band

638   towards the surrounding rock mass. Conversely, a thicker band will produce less heat and

639   excess pore pressure, which will take longer to dissipate. The maximum velocity reached is

640   similar to the calculated velocity for a case in which no thermal effects are included (also

641   plotted in Figure 5). For values of Σ lower than 10^{-7}, no effect of Ψ and Σ is observed and the

642   maximum velocity is the same in all cases. The case of zero thickness shear band is also

643   included in the plot. No significant differences are observed when compared with finite

644   thickness bands.

645   Parameter Σ, which controls the dissipation of excess pore pressure is key in determining the

646   response of the slide. Values of Σ above 10^{-3} result in almost no heat-induced effect. Thermally

647   induced excess pore pressure can dissipate quickly in these cases and frictional strength

648   remains slightly smaller than the initial value. The ratio between the shear strength remaining

649   after the maximum runout has been reached and the initial shear strength is plotted in Figure

650   6. The shear strength essentially vanishes for values of Σ below 10^{-7}, while for values above

651   10^{-3} it maintains its initial value.

652   It is concluded that the effect of the dimensionless parameter Ψ, which essentially varies with

653   the thickness of the shear band, is quite limited.

654   Parameter Σ combines permeability and band compressibility. However the effect of

655   compressibility cannot be accounted for exclusively by Σ because parameter Π is inversely

656   proportional to compressibility: it controls the development of pore pressures for a given heat

657   input, which is an effect independent from pore pressure dissipation, which is governed by Σ.

658   An additional set of calculations were performed to show the combined effect of permeability

659   and compressibility for constant $\Psi=345$, which corresponds to a shear band thickness

660    $2e=5mm$. The selected values for parameter Π imply a wide, about two orders of magnitude,

661   range of variability of the soil compressibility. The values of **Error! Reference source not**

662   **found.** are used for the remaining parameters. The results are plotted in Figure 7.

663   Figure 7 shows, as well as Figure 5b for $\Pi=1$, that there is a range of dimensionless

664   consolidation coefficients Σ that separates a high velocity regime (for low Σ values) from a low

665   velocity-, no-heat effect regime (for high Σ values). The observed trends in the variation of

666   velocity with parameter Σ are similar for all Π values. Reducing Π, i.e. increasing band

667　stiffness, decreases the threshold Σ range separating high and low velocity regimes. In other

668　words, given a value of Σ, lower values of Π, which control the heat induced pore water

669　pressure, result in lower sliding velocity.

670　<u>Rate dependent friction</u>

671　Consider now the effect of rate dependent friction. Material properties given in **Error!**

672　**Reference source not found.** have also been adopted in the cases presented in this section. A

673　base case for discussion is defined by using the frictional law of equations (18) and (19), for A =

674　$4.7 \cdot 10^{-3}$ and a reference velocity $\hat{v}_{ref} = 6.4 \cdot 10^{-7}$. The effect of these parameters on the gain in

675　strength with velocity is plotted in Figure 8. This rate dependent law is within the range of

676　experimental results measured at low to moderate shearing velocities (say, below 0.1m/s).

677　Above this velocity thermal pressurization and other phenomena discussed before contribute

678　to the measured rate dependence. However, the plot is extended to high velocities to show

679　the maximum contribution which may be expected from rate effects at high shearing speeds.

680　The parameters chosen imply an increment of 7%, close to one degree, for high sliding velocity

681　(30 m/s). The rate dependent strength increases quickly at low velocity and then levels off.

682　Results for a different value of parameter A, used in the discussion below, are also plotted in

683　Figure 8.

684　The slide is destabilised by imposing a 1m increment of the water level. This reduces the SF

685　from 1 to 0.98. Limit equilibrium for this water level is reached for a friction angle equal to

686　12.32º, 2.7% higher than the static friction angle associated with velocities lower than the

687　reference creeping velocity.

688　The base case was analyzed for different values of the Π and Σ parameters. The band

689　thickness-controlled parameter Ψ is considered constant and equal to 345, as its effect has

690　been shown to be insignificant. The results in terms of maximum dimensionless velocity are

691　plotted in **Error! Reference source not found.**. The case where thermal effects are ignored is

692   added to the figure; in that case dynamic equilibrium is reached for a dimensionless velocity of

693    $4.6 \cdot 10^{-5}$ equivalent to $7.2 \cdot 10^{-4}$ m/s, a reference velocity that depends only on the safety factor

694   attained immediately after the initial instability (Equation 1).

695   When thermal effects are considered, the response observed is similar for the different values

696   of parameter Π selected. A narrow range of Σ values separates fast and slow sliding regimes. If

697   compared with the no-rate-effect case (Figure 5b) the calculated sliding velocities are now

698   higher. This is a consequence of the stronger initial trigger imposed to initiate the slide run-out

699   (Δh_w is now 1 m against Δh_w=0.1m in the previous case).

700   The effect of parameter Π is similar to the effect observed in cases were rate effects were not

701   included. However, the threshold range of Σ values separating the slow and fast sliding

702   regimes decreases when a rate effect on friction is included. This becomes apparent by

703   comparing Figures 9 and 7. In other words, rate effects extend the range of "safe" cases, i.e. of

704   slopes that will not accelerate due to thermal pressurization effects. It appears also that the

705   threshold Σ range is narrower in Figure 9 (rate effects included), compared with Figure 6 (no

706   rate effects)

707   Figure 10 presents the maximum temperature in the centre of the shear band for the cases

708   plotted in Figure 9. If the landslide reaches a high velocity quickly, as is the case for Σ lower

709   than 10^{-9}, the shearband temperature remains relatively low. The temperature also remains

710   low, almost constant, in those cases where the velocity remains low, in a creeping mode, when

711   Σ is higher than 10^{-5}. Maximum values of temperature are reached in intermediate cases,

712   where the excess pore pressure rises relatively slowly and the velocity, although it may

713   eventually become very high, increases at a slower pace. The acceleration of the slide is in fact

714   a critical factor controlling the development of temperature.

715   Increasing the rate dependent component of friction has been shown to have a significant

716   effect in reducing the threshold permeability (through Σ) that leads to a fast sliding regime.

717   This is further shown in Figure 11 where the maximum velocity is plotted in terms of Σ for

718   three *A* values (see Figure 8 for their effect on friction increase). In all cases Ψ=345 and Π=1.0.

719   As expected, the creep velocity when thermal effects are ignored (or Σ has a high value)

720   decreases for increasing *A*. It is noted that for relatively low values of Σ, when excess pore

721   pressure dissipation is slow, the maximum velocity attained is similar in all cases irrespective of

722   the considered rate dependence of friction. When thermal effects develop they dominate the

723   sliding behaviour. However, the development of heat induced pore pressure build-up depends

724   on the creeping history. This relevant issue is discussed in more detail in the next section.

725   5.3 Evolution of motion. Creep-thermo-mechanical interactions

726   Attention is now focused on the effect of the rate of friction increase on the blow-up time, i.e.

727   the time after initiation at which the slope enters a final catastrophic phase. Calculations are

728   performed for a planar slide with D=240m, base friction angle of 12º and slope angle of 9.8º An

729   unbounded domain is assumed and a maximum runout of 2D=480m is considered.

730   To investigate the effect of the rate parameter *A*, a set of analyses is run where the slide is

731   triggered by a minuscule increase of h_w by 0.025% above the strict equilibrium value, resulting

732   to a change in the safety factor $\delta SF = 6 \cdot 10^{-5}$. In the case of rate-independent friction (i.e.

733   *A*=0) catastrophic failure occurs immediately; the slide is classified as "rapid" (IUGS, 1995) 2sec

734   after initiation and, within a few more seconds, frictional heating leads to high temperature

735   and excess pore pressure almost equal to the overburden stress.

736   The introduction of even a very mild rate effect, e.g. *A*=10^{-5} corresponding to a negligible

737   increase in friction angle by 0.01^{0} for a 10^{4}-fold increase in velocity, suppresses catastrophic

738   acceleration and leads to creep at constant velocity. The magnitude of the velocity attained is

739   governed by the rate parameter *A*; for *A*=10^{-5} it is 22cm/day and drops to 1.5cm/day for

740   *A*=10^{-3}, classifying both slides as "slow" (IUGS, 1995). The temperature increases by 10^{0}C or

741   less and the excess pore pressure generated is negligible.

742   To further explore the effect of the rate parameter a second set of analyses is run, where the

743   slide is triggered by a more substantial increase of the groundwater level, resulting to

744    $SF = 0.99$. Figure 12 summarises the results.

745   In the case of rate-independent friction *A*=0 but also for any $A \leq 10^{-4}$, high temperature and

746   excess pore pressure occur almost immediately and lead to catastrophic failure. For

747    $A = 5 \cdot 10^{-4}$ a transitional behaviour is observed, where the slide first creeps with near-

748   constant velocity for the first 15sec before accelerating to catastrophic failure, while for

749    $A > 5 \cdot 10^{-4}$ the slide creeps with "moderate" (IUGS, 1995) constant velocity. Therefore a

750   threshold value A$_{crit}$ of the rate parameter must exist, that determines whether catastrophic

751   acceleration will occur; in this case $6 \cdot 10^{-4} > A_{crit} > 5 \cdot 10^{-4}$. This is further explored using

752   models for a range of values in this interval. Figure 12 shows that even small changes, of the

753   order of 2%, of the rate parameter can have order-of magnitude impact on the duration of the

754   creep phase, although the predicted creep velocity is less sensitive. For comparison, Figure 12

755   also presents the baseline velocity, i.e. the constant creep velocity each slide would attain if

756   thermal effects were ignored: it is evident that, even where thermal effects do not eventually

757   lead to catastrophic collapse, they still increase slide velocity by at least one order of

758   magnitude.

759   It is also interesting to note that it is the *rate* of temperature increase that controls excess pore

760   pressure generation, and thus the associated loss of strength that leads to catastrophic failure.

761   If the time scale of heat generation is large enough the induced excess pore pressures may

762   dissipate before thermal pressurization occurs, irrespectively of how high the temperature

763   attained is. For a given rate of heat production, the rate of excess pore pressure generation

764   will depend on soil permeability. It is thus expected that permeability, therefore the value of

765   parameter Σ, will influence both the creep velocity and the timing of a possible catastrophic

766   failure.

767   To further investigate the impact of parameter Σ, a set of analyses is run with the same trigger,

768   rate parameter $A = 5.75 \cdot 10^{-4}$ and Σ varying between $\Sigma = 6 \cdot 10^{-8}$ and $\Sigma = 6 \cdot 10^{-13}$. The

769   results are summarised in Figure 13.

770   Lower values of Σ lead to faster development of excess pore pressure and earlier onset of a

771   catastrophic phase. As Σ increases so does the duration of the pre-failure creep phase; this

772   relationship is highly nonlinear and, as was the case for the rate parameter, a threshold value

773   Σ_{crit} exists above which a catastrophic phase is never reached. In this case $\Sigma_{crit} \cong 6 \cdot 10^{-11}$;

774   note how, close to that value, increasing the value of Σ by just 2% results to an increase in the

775   duration of the creep phase by a factor of almost three. Figure 13 further shows that, for the

776   parameters used here, the velocity of the slide during the creep phase is essentially unaffected

777   by the permeability; the baseline velocity is again plotted for comparison.

778   Finally, it was found that the maximum temperature that develops in the shearband increases

779   with permeability, regardless of whether a catastrophic phase is eventually reached. This is a

780   direct consequence of the strong influence of permeability on the rate of excess pore pressure

781   generation: the lower the permeability, the faster excess pore pressure rises and effective

782   stress drops, therefore reducing the rate of energy dissipation into heat. Conversely, the

783   higher the permeability the higher the rate of heat production necessary to achieve

784   pressurisation; in fact, models that do not predict a final catastrophic phase consistently attain

785   higher shearband temperature than models that do.

786   5.4. Compound geometry. Creep-thermo-mechanical interactions

787   Previous sections analyze the landslide evolution including two phenomena that work in

788   opposite directions: the heat-driven acceleration of the landslide and the stabilizing effect of

789   friction rate effects. In a planar geometry the slide remains always in motion. The creeping

790   velocity, away from blowup, depends on the magnitude of the destabilization factors, the

791   intensity of rate effects and additional properties of the shear band, notably its permeability.

792   But other sliding geometries are common. A good example is Vaiont, which may be

793   conceptualized as an evolutionary two-block mechanism (Pinyol and Alonso, 2010b). The

794   sliding motion results in a reduction of the mass of the upper unstable wedge and a parallel

795   increase of the mass of the stabilizing lower wedge. This is a self-stabilizing mechanism unlike

796   the single block case. The effect of this major change in the kinematic description of the

797   landslide is explored here.

798   Consider the two-block mechanism given in Figure 14. The interaction between the two sliding

799   blocks is given by the axial force on the hinged "rod" connecting the blocks. Changes in water

800   pressure act only on the lower block. In the cases solved both wedges have the same thickness

801   but different initial length. Equations of dynamic equilibrium were written for the two

802   interacting blocks. Balance equations (water flow, energy) were formulated for each of the

803   two blocks, following the previous discussion. A zero-thickness band was adopted in the two

804   blocks. The following example was analyzed: Block thickness, 25 m; the upper and lower blocks

805   have lengths of 60 m and 120 m and slide on a plane inclined 37º and 0º respectively. The

806   remaining physical constants are identical to the planar slides analyzed previously. The

807   stiffness coefficient, m_v=1.5·10^{-9} Pa^{-1}. It leads to the following constant dimensionless

808   parameters for the case analyzed: Θ=1.27·10^{-9}, Ψ=2.72·10^{7} and Π=1. The landslide is

809   destabilised by increasing the water pressure on the sliding surface of the lower block ($\hat{p}_{wh}$

810   increases by 0.04 which is equivalent to increasing the water level by 1m).

811 The calculated evolution of velocity and run-out if no friction rate effects are considered is

812 given in Figure 15. The effect of Σ, which depends on permeability in the vicinity of the shear

813 band, is highlighted. Low values, below $1.63 \cdot 10^{-7}$ m/s, lead to a slide blowup. This is also the

814 case of a planar slide. However, the main difference of the compound mechanism is that the

815 slide is able to stop, for high band permeability, as a consequence of the weight transfer

816 between upper and lower blocks. Note also that the thermal effect results in some increase of

817 the run-out and velocity if compared with the no thermal pressurization analysis.

818 Friction rate effects, for the same case, are shown in Figure 16 (A = $4.7 \cdot 10^{-3}$). If conditions lead

819 to thermal blowup, rate effects and slide geometry become largely irrelevant in controlling the

820 sliding velocity and run-out. However, if blowup conditions are not attained, rate effects play a

821 significant role: they reduce the Σ threshold between fast and creeping regimes of the slope

822 and run-out and velocity during the transient motion of the slide after initial instability is

823 significantly   reduced.   This   becomes   apparent   by   comparing   Figures   15   and   16.

824

825 6. CONCLUSIONS

826

827 Known cases of rapid landslides can only be explained by negligible shear strength acting on

828 the main failure surface. Among the proposed mechanisms of strength reduction, thermal

829 pressurization of pore water in saturated shear bands may explain a fast accelerated motion as

830 well as a transition from creeping to fast regimes in cases of landslide reactivation. Measured

831 strain rate effects on friction, at low to moderate shearing rates, suggest a linear increase in

832 friction with the logarithm of shearing velocity, a relationship supported by basic friction

833 concepts.

834 A dynamic modelling of landslide motion, which integrates strain rate effects and thermal

835 interactions in a deforming shear band, provides considerable insights into the evolution of the

836 sliding velocity and its eventual blowup, when thermal pressurization dominates the slide

837 motion. A model of this kind, initially developed for planar landslides, has been described by a

838 set of dimensionless balance and equilibrium equations. Four dimensionless constitutive

839 coefficients which control the slide movement were derived. It was found that the shear band

840 permeability and, to a lesser extent, its compressibility, dominate the entire phenomenon.

841 The set of equations require a numerical solution. A novel staggered implicit integration

842 procedure has been proposed. It is capable of handling, within reasonable computational

843 times, a long creeping history and a sudden final blowup.

844 Transition from a slow creeping-like motion to fast acceleration is quite sharp in terms of a

845 dimensionless "consolidation" coefficient which relates band permeability and stiffness as well

846 as the height of the sliding mass. This threshold is significantly affected by friction rate effects

847 in the sense that increasing rate effects reduces the range of shear band properties leading to

848 blowup phenomena. Given a creeping motion of a specific landslide, time to blowup is very

849 sensitive to strain rate effects. Beyond a certain value of the rate parameter, blowup does not

850 seem to be possible within realistic runout distances.

851 The paper also examines the behaviour of compound slide geometries, in particular those

852 consisting of a self-stabilizing mechanism. If blowup conditions develop the slide accelerates as

853 much as a planar slide. However, the creeping stage is also controlled, in addition to aspects

854 valid for planar slides, by geometrical details and the evolutionary changes in slide geometry.

855 Finally, although the intention of the paper was to provide a theoretical investigation of the

856 problem rather than an analysis of a specific landslide, the models presented can be readily

857 used on appropriate real cases, at least as a back-analysis tool. Predictive modelling is also

858 possible in principle; however a pertinent issue in this respect is the calibration of material

859 parameters, especially the rate parameter, which may have significant impact on predictions.

860

861   REFERENCES

862

863

864   Alcántara-Ayala, I. & Domínguez-Morales, L. (2008). The San Juan de Grijalva catastrophic

865   landslide, Chiapas, Mexico: lessons learnt. *Web Proceedings of the First World Landslide*

866   *Forum.* International Consortium on Landslides. United Nations International Strategy for

867   Disaster Reductions. Nicola Casagli, Riccardo Fanti, Veronica Tofani (eds.). Tokyo, Japan, 96-

868   99.

869   Alonso, E. E., & Pinyol, N. M. (2014). Slope stability in slightly fissured claystones and marls.

870   *Landslides*. Published online.

871   Alonso, E., Pinyol, N. & Puzrin, A. (2010). *Geomechanics of Failures. Advanced Topics*, Springer.

872   Alonso, E.E., Pinyol, NM & Yerro, A (2014). Mathematical Modelling of Slopes. *Procedia Earth*

873   *and Planetary Science* **9**, 64–73.

874   Campbell, C.S., Cleary, P.W. & Hopkins, M.A. (1995). Large-scale landslide simulations: global

875   deformation, velocities, and basal friction. *J. Geophys. Res. Solid. Earth* **100**, No. B5, 8267–

876   8283.

877   Andersen, S. & Andersen, L. (2010). Modelling of landslides with the material-point method.

878   *Computational Geosciences* **14**, No. 1, 137–147.

879   Bardenhagen, S.G. & Kober, E.M. (2004). The generalized interpolation material point method.

880   *Computer Modeling in Engineering and Sciences* **5**, No. 6, 477–495.

881   Bishop A. W. (1971). The influence of progressive failure on the choice of the method of

882   stability analysis. *Géotechnique* **21**, 168–172.

883   Bishop, A. W. (1967). Progressive failure-with special reference to the mechanism causing it.

884   *Proceedings of the Geotechnical Conference*, *Olso*, Vol. 2, 142–150.

885   Bjerrum L (1967). Progressive failure in slopes of overconsolidated plastic clay and clay- shales.

886   *J. Soil. Mech. Fdn. Div. Am. Soc. Civ. Eng.* **93**, No. SM5, 3–49.

887   Bowden, F. & Tabor, D (1964). *The friction and lubrication of solids*. New York. Oxford

888   University Press.

889   Cascini, L., Cuomo, S., Pastor, M., & Sorbino, G. (2010). Modeling of Rainfall-Induced Shallow

890   Landslides of the Flow-Type. *Journal of Geotechnical and Geoenvironmental Engineering* **1**

891   No. January, 85–98.

892   Cecinato, F. & Zervos, A. (2012). Influence of thermomechanics in the catastrophic collapse of

893   planar landslides. *Canadian Geotechnical Journal* **49**, No. 2, 207–225.

894   Cecinato, F., Zervos, A. & Veveakis, E. (2011). A thermo-mechanical model for the catastrophic

895   collapse of large landslides. *Int. J. Numer. Anal. Meth. Geomech.* **35**, 1507-1535.

896   Chamot, P. (1993). El deslizamiento La Josefina en el Valle del Tío Paute. Report to the United

897   Nations, 16p.

898   Chen, T. C., Lin, M. L., & Hung, J. J. (2003). Pseudostatic analysis of Tsao-Ling rockslide caused

899   by Chi-Chi earthquake. *Engineering Geology* **71**, No.1-2, 31–47.

900   Cleary, P. W. & C. S. Campbell (1993). Self-lubrication for Long Runout Landslides: Examination

901   by computer simulation. *J. Geophys. Res*. **98**, No. B12, 21911–21924.

902   Conte, E., Silvestri, F. & Troncone, A. (2010). Stability analysis of slopes in soils with strain-

903   softening behaviour. *Computers and Geotechnics* **37**, No. 5, 710–722.

904   Cooper, M. (1996). The progressive development of a failure slip surface in over-consolidated

905   clay at Selborne, UK. *7th Int. Symp. on Landslides.* Trondheim, Norway. Senneset, K. (ed.),

906   Balkema, 683–688.

907   Cooper, M.R., Bromhead, E.N., Petley, D.J. & Grant, D.I. (1998). The Selbourne cutting stability

908   experiment. *Géotechnique* **48**, No. 1, 83–101.

909   Dai, F.C, Deng, J.H., Tham, L.G., Law, K.T. & Lee, C.F. (2004). A large landslide in Zigui County,

910   Three Gorges area. *Canadian Geotechnical Journal* **41**, 1233-1240.

911   Darve, F. & Laouafa, F. (2000). Instabilities in granular materials and application to landslides.

912   *Mech. Cohes.-Frict. Mater.* **5**, 627–652.

913   Davis R.O., Desai, C.S. & Smith, N.R. (1993). Stabiltiy of motions of translatinoal landslide.

914   *Journal of Geotechnical Engineering* **119**, No. 3, 420-432.

915   De Blasio, F. V. (2008). Production of frictional heat and hot vapour in a model of self-

916   lubricating landslides. *Rock Mechanics and Rock Engineering* **41**, 219–226.

917   Di Toro, G., Hirose, T., Nielsen, S., Pennacchioni, G., & Shimamoto, T. (2006). Natural and

918   experimental evidence of melt lubrication of faults during earthquakes. *Science* **311**, No.

919   February, 647–649.

920   Dieterich, J. (1979) Modeling of rock friction 1. Experimental results and constitutive

921   equations. *Journal of Geophysical Research* **84**, No. B5, 2161-2168.

922   Dounias GT, Potts DM and Vaughan PR (1996). Analysis of progressive failure and cracking in

923   old British dams. *Géotechnique* **46**, No. 4, 621–640.

924   Dowell, M. & Jarratt, P. (1972). The "Pegasus" method for computing the root of an equation.

925   *BIT* **12**, 503-508.

926   Duncan, J. (1996). State of the Art: Limit Equilibrium and Finite-Element Analysis of Slopes. *J.*

927   *Geotech. Engrg.* **122**, No. 7, 577–596.

928   Ferri, F., Di Toro, G., Hirose, T., & Shimamoto, T. (2010). Evidence of thermal pressurization in

929   high-velocity friction experiments on smectite-rich gouges. *Terra Nova* **22**, No. 5, 347–353.

930   Follacci, J.-P., L. Rochet & J.-F. Serratrice (1993). Glissement de La Clapière, St. Etienne de

931   Tinée, Synthèse des connaissances et actualisation des risques,

932   rapp.92/PP/UN/I/DRM/03/AI/01, 76 pp., Cent. Etud. Tech. de l'Equip., Nice, France.

933   Gens, A. & Alonso, E.E. (2006). Aznalcóllar dam failure. Part 2: Stability conditions and failure

934   mechanism. *Géotechnique* **56**, No. 3, 185–201.

935   Goguel, J. (1978) Scale-dependent rockslide mechanisms, with emphasis on the role of pore

936   fluid vaporization. *Rockslides and avalanches.* Voight, B. (ed.) Elsevier, Amsterdam, 693–

937   706.

938   Goren, L. & Aharonov, E. (2007). Long runout landslides: The role of frictional heating and

939   hydraulic diffusivity. *Geophysical Research Letters* **34**, No. L07301, 1–7.

940   Goren, L. & Aharonov, E. (2009). On the stability of landslides: A thermo-poro-elastic approach.

941   *Earth and Planetary Science Letters* **277**, No. 3-4, 365–372.

942   Goren, L. & Aharonov, E. (2009). On the stability of landslides: A thermo-poro-elastic approach.

943   Earth and Planetary Science Letters, 277(3-4), 365–372.

944   Goren, L., Aharonov, E. & Anders, M. H. (2010). The long runout of the Heart Mountain

945   landslide: Heating, pressurization, and carbonate decomposition. *Journal of Geophysical*

946   *Research: Solid Earth* **115**, No. B10, 1–15.

947   Habib, P. (1975) Production of gaseous pore pressure during rock slides. *Rock. Mech. Rock.*

948   *Engng*. **7**, 193–197.

949   Han, R., & Hirose, T. (2012). Clay-clast aggregates in fault gouge: An unequivocal indicator of

950   seismic faulting at shallow depths?. *Journal of Structural Geology* **43**, No. October, 92–99.

951   Harden, C.P. (2004). The 1993 Landslide dam at La Josefina in Southern Ecuador: A review of

952   "Sin plazo para La Esperanza". *Engineering Geology* **74**, No. 1-2, 157-161.

953   He, S.-M., Liu, W. & Wang, J. (2015). Dynamic simulation of landslide based on thermo-poro-

954   elastic approach. *Computers & Geosciences* **75**, No. February, 24–32.

955   Helmstetter A., Sornette D., Grasso J. R., Andersen J. V., Gluzman S &, Pisarenko, V. (2003)

956   Slider-block friction model for landslides: application to Vajont and La Clapière landslides. *J.*

957   *Geophys. Res*. **109**, No. B02409.

958   Hendron, A.J. & Patton, F.D. (1985). The Vaiont slide, a geotechnical analysis based on new

959   geologic observations of the failure surface. *Technical Report GL−85−5*. Department of the

960   US Army Corps of Engineers, Washington, DC.

961   Hewitt, K., Clague, J. J., & Orwin, J. F. (2008) Legacies of catastrophic rock slope failures in

962   mountain landscapes. *Earth-Science Reviews* **87** (2008), 1–38.

963 HSL. A collection of Fortran codes for large scale scientific computation.
964   http://www.hsl.rl.ac.uk/

965 HSL. A collection of Fortran codes for large scale scientific computation.
966   http://www.hsl.rl.ac.uk/ (accessed February 2015).

967 Hungr, O., Leroueil, S. & Picarelli, L. (2014). The Varnes classification of landslide types, an
968   update. *Landslides* **11**, 167–194.

969 IUGS - International working group, L. (1995). A suggested method for describing the rate of
970   movement of a landslide. *Bulletin of the International Association of Engineering Geology*
971   **52**, 75-78.

972 Iverson, R. M., Reid, M. E. & Lahusen, R. G. (1997). Debris-flow mobilization from landslides.
973   *Annu. Rev. Earth Planet Sci.* **25**, 85–138.

974 Leroueil, S. (2001). Natural slopes and cuts: movement and failure mechanisms. *Géotechnique*
975   **51**, No. 3, 197-243.

976 Liao, C. J., Lee, D. H., Wu, J. H., & Lai, C. Z. (2011). A new ring-shear device for testing rocks
977   under high normal stress and dynamic conditions. *Engineering Geology* **122**, No. 1-2, 93–
978   105.

979 Mesri, G., and Shahien, M. (2003). Residual shear strength mobilized in first-time slope
980   failures. *J. Geotech. Geoenviron. Eng.* **129**, No. 1, 12-31.

981 Mitchell, J.K. 1976. *Fundamentals of soil behaviour.* New York. John Wiley & Sons.

982 Mizoguchi, K., Hirose, T., Shimamoto, T., & Fukuyama, E. (2007) Reconstruction of seismic
983   faulting by high-velocity friction experiments: An example of the 1995 Kobe earthquake.
984   *Geophysical Research Letters* **34**, No. August, 2–4.

985 Müller, L. (1964). The rock slide in the Vajont Valley. *Rock Mechanics and Engineering Geology*
986   **2**, 148–212.

987 Nonveiller, E. (1987). The Vajont reservoir slope failure. *Engineering Geology* **24**, 493–512.

988   Paronuzzi, P., Rigo, E. & Bolla, A. (2013). Influence of filling–drawdown cycles of the Vajont

989   reservoir on Mt. Toc slope stability. *Geomorphology* 191, 75–93.

990   Pastor, M., Blanc, T., Haddad, B., Drempetic, V., Morles, M. S., Dutto, P., Stickle, M.M, Mira, P.

991   & Merodo, J. A. (2014). Depth Averaged Models for Fast Landslide Propagation:

992   Mathematical, Rheological and Numerical Aspects. *Archives of Computational Methods in*

993   *Engineering* **22**, No. 1, 67–104.

994   Pinyol, N. M. & Alonso, E. E. (2010a). Criteria for rapid sliding II*. Engineering Geology* **114**, No.

995   3-4, 211–227.

996   Pinyol, N. M. & Alonso, E. E. (2010b). Fast planar slides. A closed-form thermo-hydro-

997   mechanical solution. *Int. J. Numer. Anal. Meth. Geomech.* **34**, 27–52.

998   Pinyol, N. M., Alonso, E. E., Corominas, J. & Moya, J. (2011). Canelles landslide: modelling rapid

999   drawdown and fast potential sliding. *Landslides* **9**, No. 1, 33–51.

1000   Plaza-Netos, G. and Zevallos, O. (1994) The La Josefina rockslide. In The 1993 La Josefina

1001   Rockslide and Río Paute Landslide Dam. Ecuador. *Landslides News* **8**, 4-6.

1002   Potts, D.M., Dounias, G.T. & Vaughan, P.R. (1990). Finite element analysis of progressive failure

1003   of Carsington embankment. *Géotechnique* **40**, No. 1, 79−101.

1004   Rice, J. R. (2001). New perspectives in crack and fault dynamics. Mechanics for a New

1005   Millennium. *Proc. of the 20th Int. Congress of Theoretical and Applied Mechanics*. H. Aref

1006   and J. W. Phillips (eds.). Chicago. Kluwer Academic Publishers, 1-23.

1007   Rice, J. R., Lapusta, N. & Ranjith, K. (2001). Rate and state dependent friction and the stability

1008   of sliding between elastically deformable solids. *Journal of the Mechanics and Physics of*

1009   *Solids* **49**, 1865-1898.

1010   Ruina, A. (1983). Slip instability and state variable friction laws*. J. Geophys. Res.* **8**, No. B12,

1011   10359-10370.

1012   Saito M (1965). Forecasting the time of occurrence of a slope failure. *Proc. 6th Int. Conference*

1013   *on Soil Mechanics and Foundation Engineering. Montreal.* Vol. 2, 315–318.

1014   Saito, M. (1969). Forecasting time of slope failure by tertiary creep. *Proc. 7th International*

1015   *Conference on Soil Mechanics and Foundation Engineering. Mexico City.* Vol. 2*, 677–683.*

1016   Schuster, R.L., Salcedo, D.A. and Valenzuela, L. (2002). Overview of catastrophic landslides of

1017   South America in the twentieth century. *Catastrophic Landslides: Effects, Occurrences and*

1018   *Mechanism.* Evans, S.G. and DeGraff, J.V. (eds.). Geological Society of America.

1019   Semenza, E. (2001). La Storia del Vaiont Raccontata del Geologo che ha Scoperto la Frana.

1020   *Tecomproject*. Editore Multimediale. Ferrara.

1021   Skeel, R. D. (1986). Construction of variable-stepsize multistep formulas. *Mathematics of*

1022   *Computation* **47**, No. 176, October, 503-510.

1023   Skempton A.W., Petley, F.R.S and Petley, D.J. (1967). The strength along structural

1024   discontinuities in stiff clays. *Proc. of Geotechnical Conference*. *Olso, Norwegian*. Vol. 2, 55-

1025   69.

1026   Skempton, A. W. (1985). Residual Strength of Clays in Landslides, Folded Strata, and the

1027   Laboratory. *Géotechnique* **35**, No. 1, 3-18.

1028   Sosio, R., Crosta, G. B., & Hungr, O. (2008). Complete dynamic modeling calibration for the

1029   Thurwieser rock avalanche (Italian Central Alps). *Engineering Geology* **100**, 11–26.

1030   Tang, C. L., Hu, J. C., Lin, M. L., Angelier, J., Lu, C. Y., Chan, Y. C., & Chu, H. T. (2009). The

1031   Tsaoling landslide triggered by the Chi-Chi earthquake, Taiwan: Insights from a discrete

1032   element simulation. *Engineering Geology* **106** , No. 1-2, 1–19.

1033   Tika, T. E., Vaughan, P. R. & Lemos, L. (1996). Fast Shearing of Pre-Existing Shear Zones in Soil.

1034   Géotechnique **46**, No. 2, 197-233.

1035   Ujiie, K., & Tsutsumi, A. (2010). High-velocity frictional properties of clay-rich fault gouge in a

1036   megasplay fault zone, Nankai subduction zone. *Geophysical Research Letters* **37**, No.

1037   December, 1–5.

1038   Uriel Romero, S. & Molina, R. (1977). Kinematic aspects of Vaiont slide. *Proc. of the 3rd*

1039   *International Conference of the ISRMR. Denver, USA*. National Academy of Sciences 2B,

1040   865–870.

1041   Vardoulakis, I. (2000). Catastrophic landslides due to frictional heating of the failure plane.

1042   *Mechanics of Cohesive-frictional Materials* **5**, No. 6, 443–467.

1043   Vardoulakis, I. (2002). Dynamic thermo-poro-mechanical analysis of catastrofic landslides.

1044   *Géotechnique* **52**, No. 3, 157–171.

1045   Veveakis, E., Vardoulakis, I. & Di Toro, G. (2007). Thermoporomechanics of creeping landslides:

1046   The 1963 Vaiont slide, northern Italy. *Journal of Geophysical Research* **112**, No. F3, F03026.

1047   Voight, B. (1978) *Rockslides and avalanches*, Volume 1, New York, Elsevier.

1048   Voigt, B. & Faust, C. (1982). Frictional heat and strength loss in some rapid landslides.

1049   *Géotechnique* **32**, No. 1, 43–54.

1050   Wagner, W. & Kruse, A. (1998). *Properties of Water and Steam.* Springer-Verlag

1051   Wang, F.W., Zhang, Y.M., Huo, A.T., Matsumoto, T. & Huang, B.T. (2004) The July 14, 2003

1052   Qianjiangping landslide, Three Gorges Reservoir, China. *Landslides* **1**, 157-162.

1053   Wedage, A., Morgenstern, N. R. & Chan, D. H. (1998). A strain rate dependent constitutive

1054   model for clays at residual strength. *Canadian Geotechnical Journal* **35**, 364–373.

1055   Więckowski, Z., Sung-Kie, Y. & Jeoung-Heum, Y. (1999). A particle-in-cell solution to the silo

1056   discharging problem. *Int. J. Numer. Anal. Meth. Geomech.* **45**, No. 9, 1203–1225.

1057   Wu, J-H. & Chen, C-H (2011). Application of DDA to simulate characteristics of the Tsaoling

1058   landslide. *Computers and Geotechnics* **38**, No. July, 741–750.

1059   Yang, C-M., Yu, W-L., Dong, J-J., Kuo, C-Y., Shimamoto T., Lee, C-T., Togo, T., Miyamoto, Y.

1060   (2014). Initiation, movement, and run-out of the giant Tsaoling landslide — What can we

1061   learn from a simple rigid block model and a velocity–displacement dependent friction law?.

1062   *Engineering Geology* **182** Part B, No. November, 158–181.

1063   Yerro, A., Alonso, E.E & Pinyol, N.M. (2014). Modelling progressive failure with MPM.

1064   *Numerical Methods in Geotechnical Engineering* NUMGE 2014, Delf. Hicks M, Brinkgreve

1065   RBJ and Rohe A (eds.). Balkema, Leiden, The Netherlands, Vol. 1, 319–323.

1066   Zabala, F. & E.E. Alonso (2011). Progressive failure of Aznalcóllar dam using the Material Point

1067   Method*. Géotechnique* **61**, No. 9, 795–808.

1068

1069   FIGURES

1070
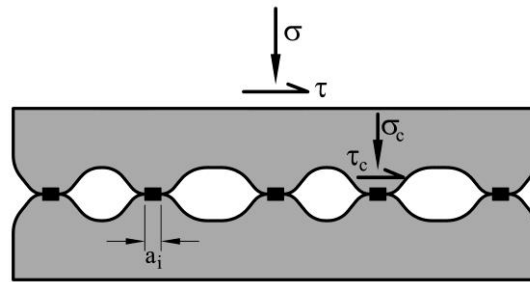
1071
1072
1073   Figure 1. Sketch to illustrate the concept of friction.

1074

1075

1076
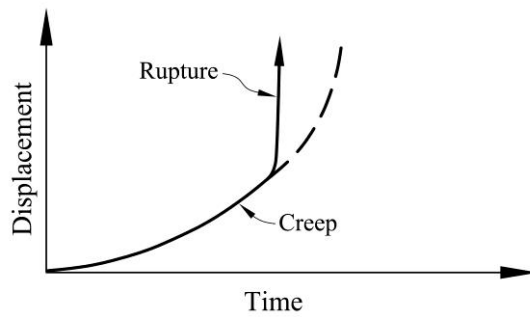
1077   Figure 2. Creep and rupture: two interacting mechanisms in action
1078

1079
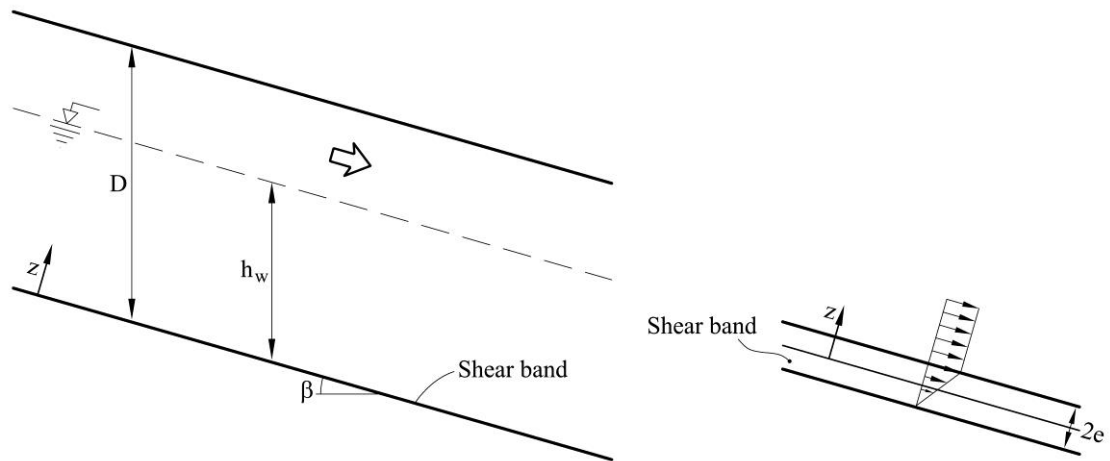
1080   Figure 3. Geometry of a planar landslide and shear band

(a)

(b)

(c)

(d)

(e)

(f)

(g)
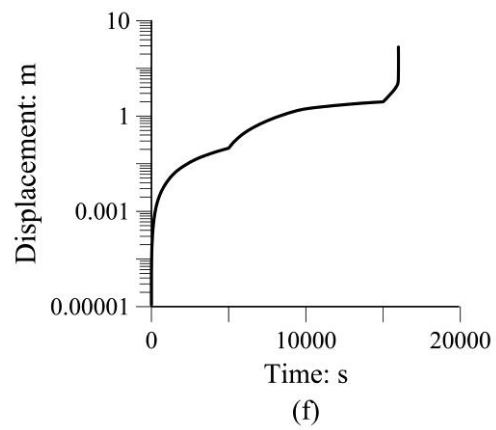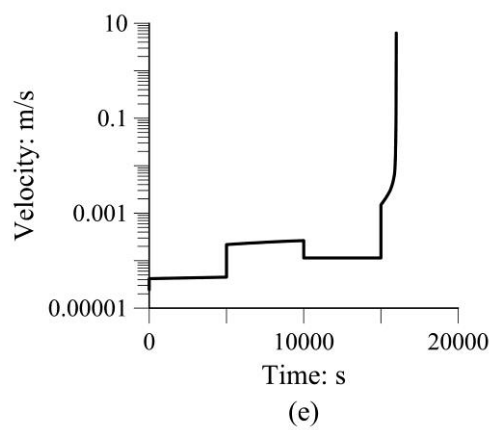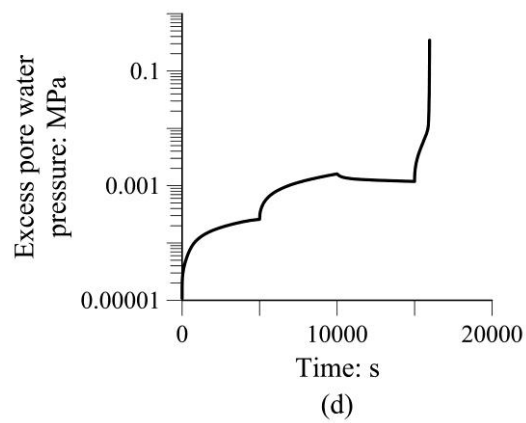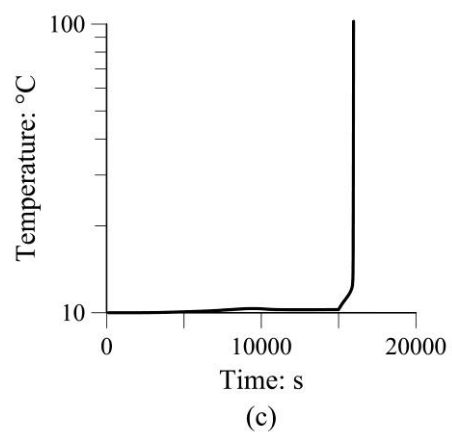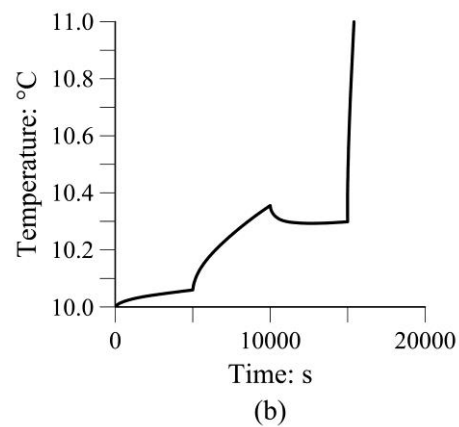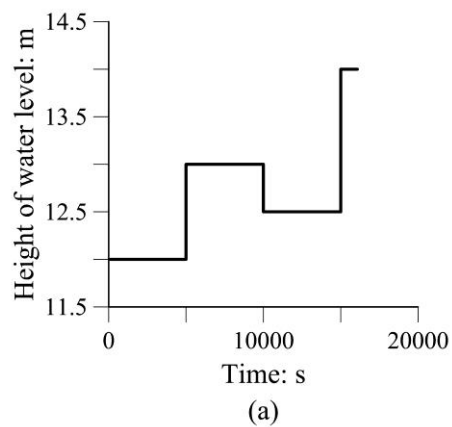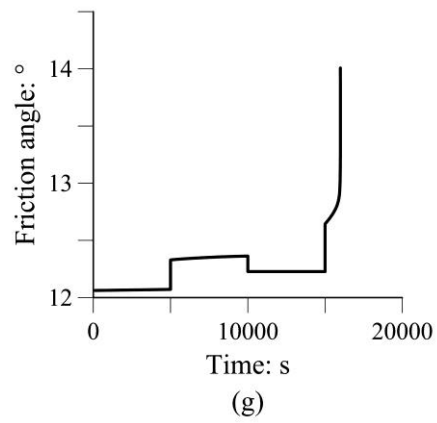
1081   Figure 4. Calculated response of an impending planar slide to an imposed variation of water level (a). (b),

1082   (c): Temperature at the center of shear band; (d): Excess pore water pressure at the center of shear

1083   band; (e): slide velocity; (f): slide displacement; (g): evolution of friction angle.

1084

1085

1086
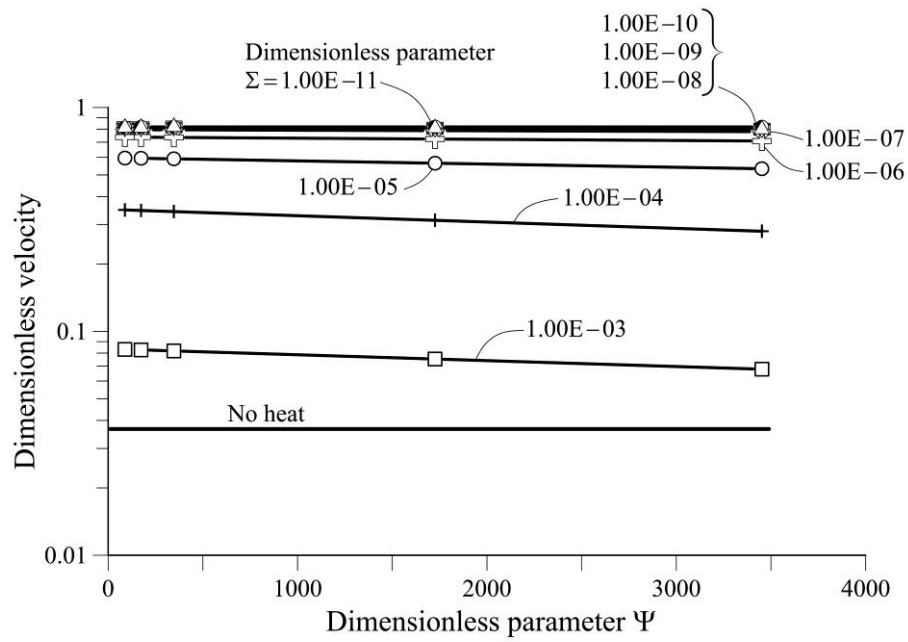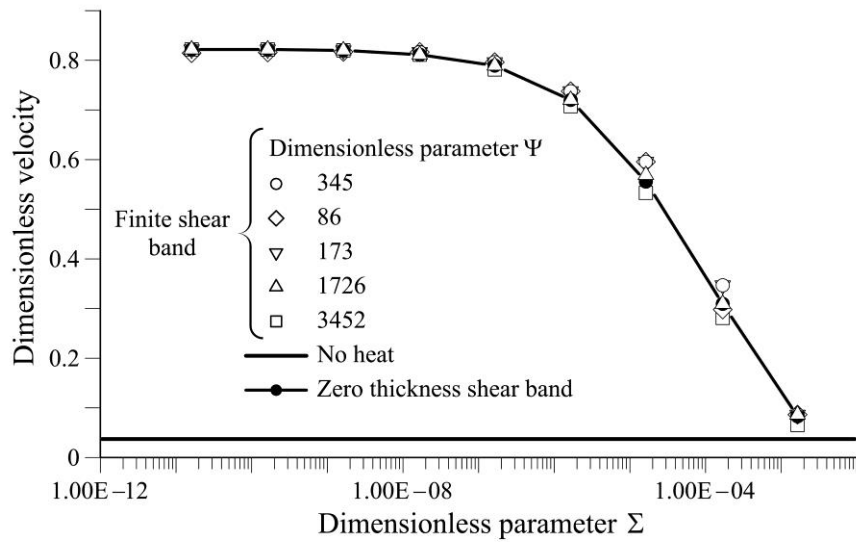
1087 Figure 5. Dimensionless velocity reached at a displacement equal to twice the height of the sliding mass
1088 for different values of two dimensionless parameters: parameters Ψ (coefficient of heat source term in
1089 the energy balance equation) and Σ, (coefficient of consolidation in the mass balance equation of water
1090 flow). Π (coefficient of rate of temperature in the mass balance equation) is equal to 1. Rate
1091 independent friction.

1092

1093

Figure 6. Ratio of final and initial shear strength for different values of two dimensionless parameters: parameter Ψ (coefficient of heat source term in the energy balance equation) and Σ (coefficient of consolidation in the mass balance equation of water flow). Π (coefficient of rate of temperature change in the mass balance equation) is equal to 1. Rate independent friction.
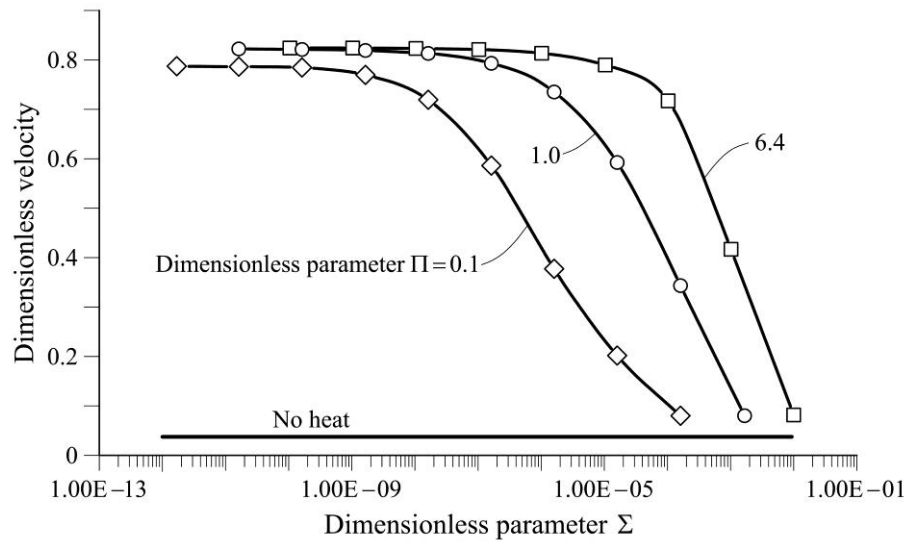
1099

Figure 7. Dimensionless velocity reached at 50 m of displacement for different values of two dimensionless parameters: parameter Π (coefficient of rate of temperature change in the mass balance equation) and Σ (coefficient of consolidation in the mass balance equation of water flow). Ψ, the coefficient of heat in the energy balance equation, is equal to 345. Rate independent friction.

1105

(a)

1106

(b)
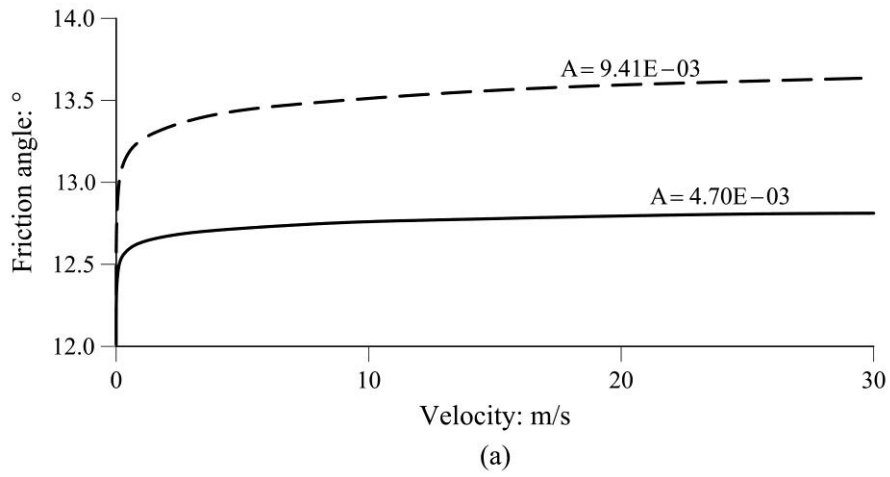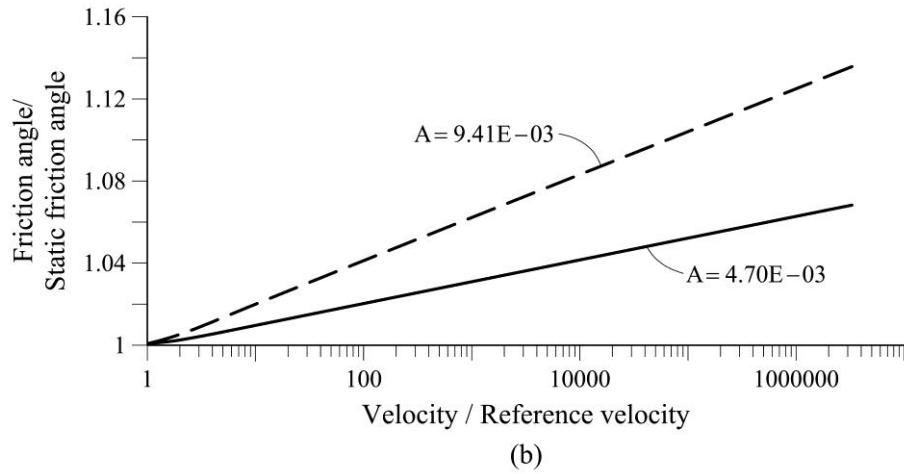
1107

1108 Figure 8. Friction angle as a function of shearing velocity for two different *A* parameters. (a) Friction
1109 angle vs velocity; (b) Ratio between friction angle and static friction angle associated with log velocity
1110 values lower than a reference vel ($\hat{v}_{ref} = 6.4 \cdot 10^{-7}$).
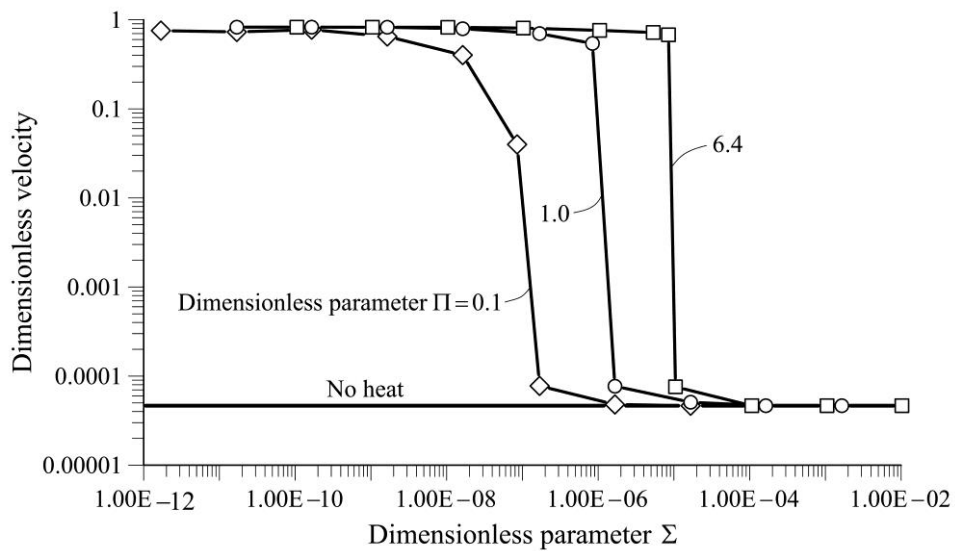
1111

1112   Figure 9. Dimensionless maximum velocity in terms of dimensionless parameters Π (coefficient of rate
1113   of temperature change in the mass balance equation) and Σ (coefficient of consolidation in the mass
1114   balance equation of water flow). Ψ (coefficient of heat source term in the energy balance equation) is
1115   equal to 345. Rate dependent friction parameters: A=4.7·10^{-3} and $\hat{v}_{ref} = 6.4 \cdot 10^{-7}$.

1116

1117
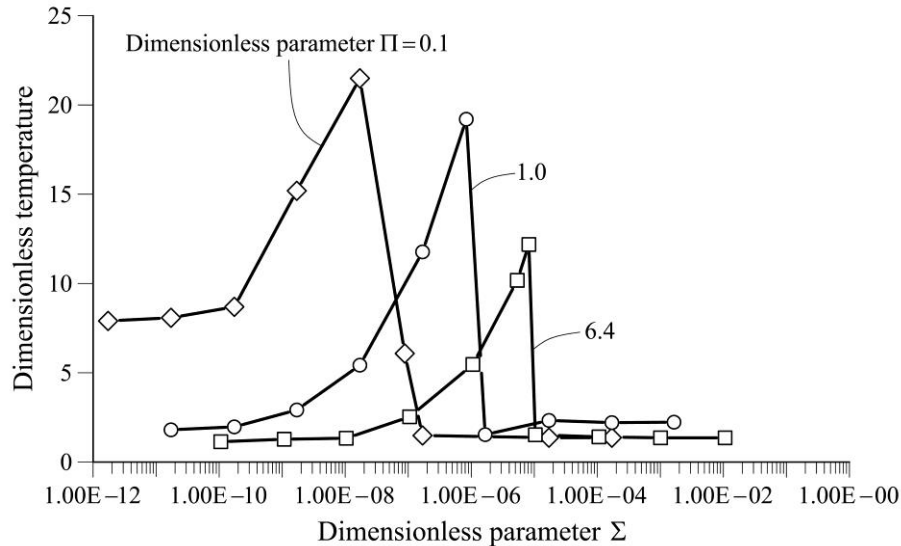
1118   Figure 10. Dimensionless temperature for different dimensionless parameters: parameter Π (coefficient
1119   of rate of temperature change in the mass balance equation) and Σ (coefficient of consolidation in the
1120   mass balance equation of water flow). Ψ (coefficient of heat source term in the energy balance
1121   equation) is equal to 345. Rate dependent friction with A=4.7·10^{-3} and a reference velocity equal to
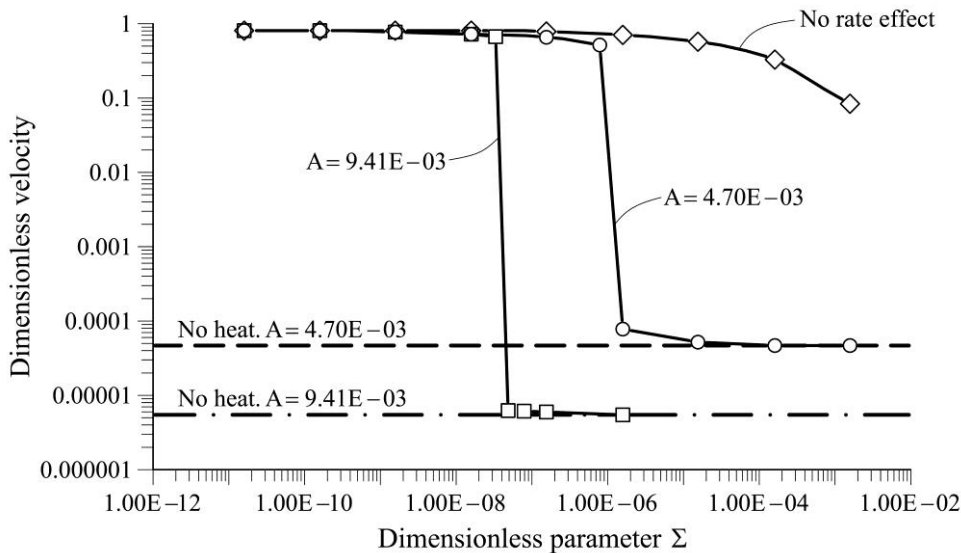1122 $\hat{v}_{ref} = 6.4 \cdot 10^{-7}$.

1123

1124   Figure 11. Dimensionless velocity in terms of dimensionless parameters Π (coefficient of rate of
1125   temperature change in the mass balance equation) and Σ (coefficient of consolidation in the mass
1126   balance equation of water flow) for three values of the rate effect parameter A. Ψ (coefficient of heat
1127   source term in the energy balance equation) is equal to 345. In all cases plotted, $v_{ref} = 10^{-5}$ m/s.
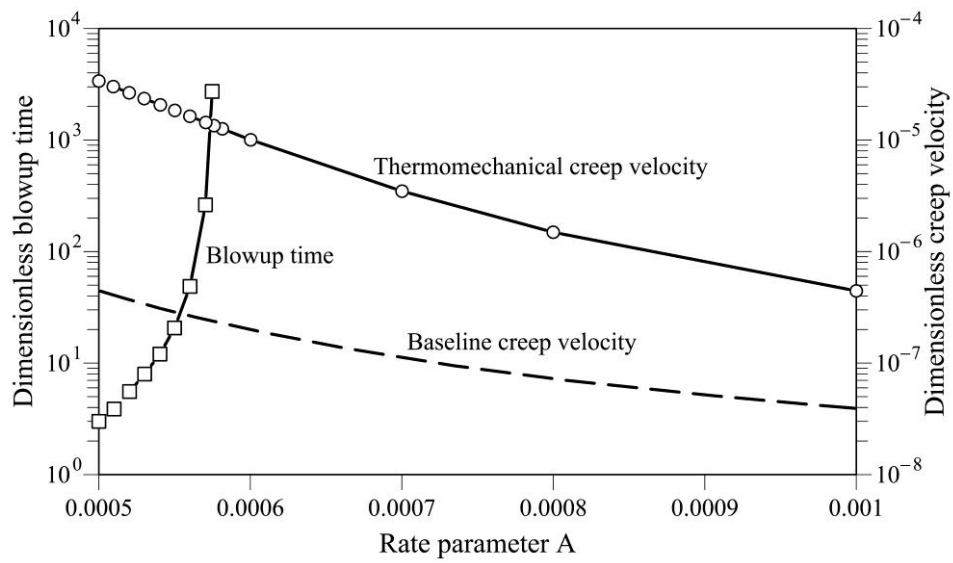
1128

1129   Figure 12. Effect of rate parameter on creep velocity and blowup time
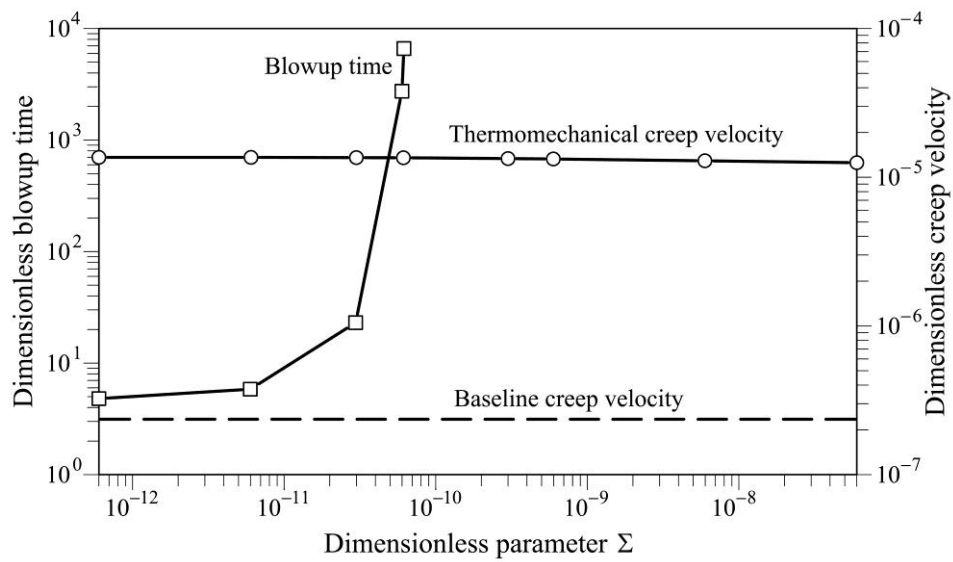
1130

1131   Figure 13. Effect of the dimensionless parameter Σ (coefficient of consolidation in the mass

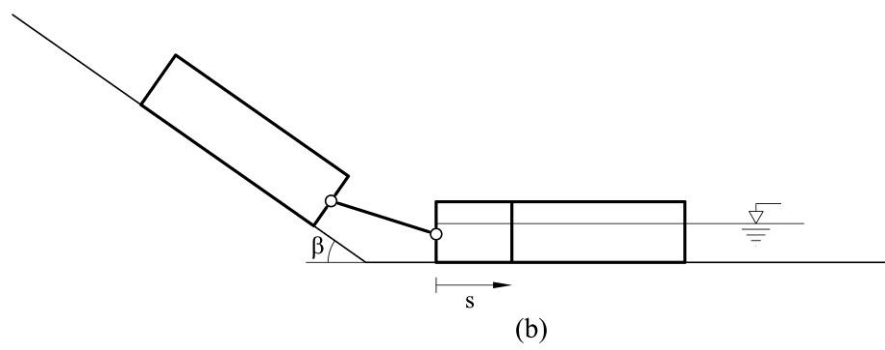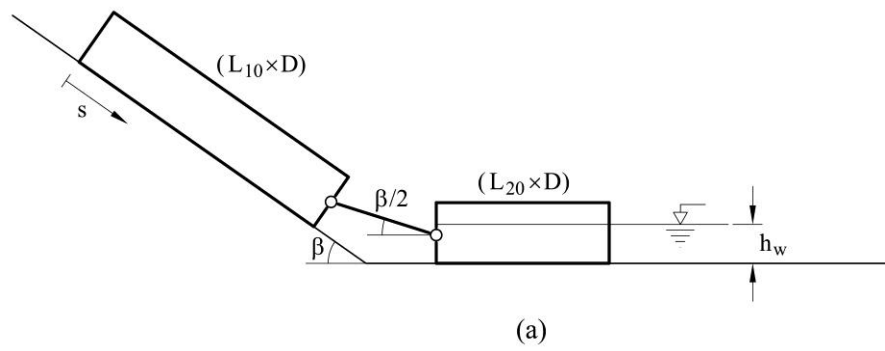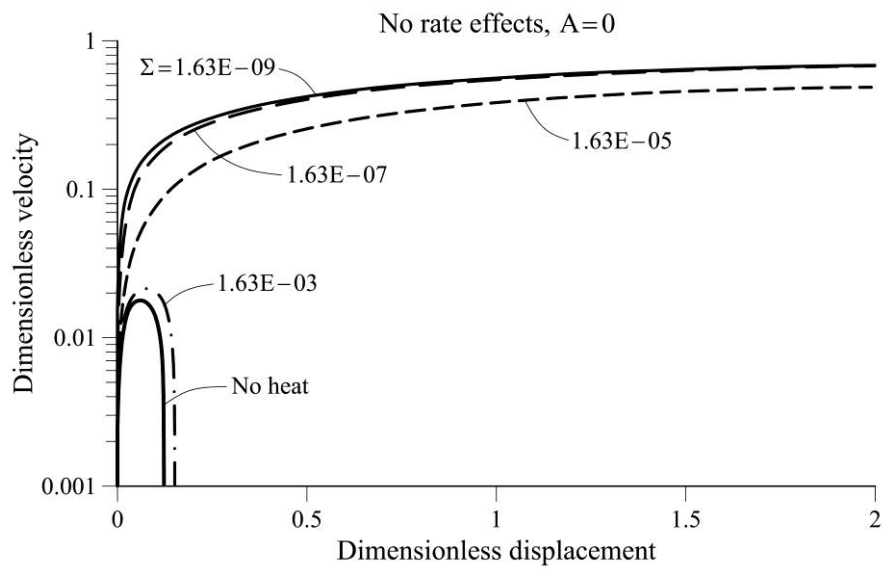1132   balance equation of water flow) on creep velocity and blowup time

1133

1134

(a)

1135

(b)

1136   Figure 14. The two-block model analysed.
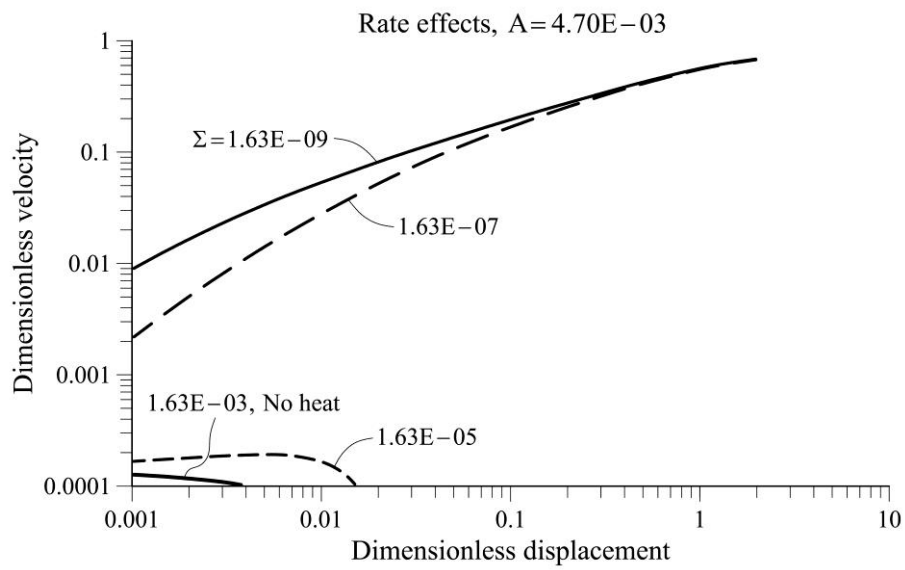
1137

1138

No rate effects, A=0

1139

1140 Figure 15. Thermal analysis of two block model; no rate effect on friction (*A*=0). Effect of

1141 dimensionless parameter Σ (coefficient of consolidation in the mass balance equation of water

1142 flow) on velocity and run-out.

1143

1144

1145

1146

Rate effects, A = 4.70E−03

1147

1148   Figure 16. Thermal analysis of two block model; rate effect on friction characterized by

1149 A=4,7·10^{-3} and a reference velocity equal to $\hat{v}_{ref} = 6.4·10^{-7}$. Effect of band permeability on

1150   velocity and run-out.

1151

TABLE

Table 1. Contributions to thermal analysis of catastrophic landslides

References	Problem description and governing equations	Sliding geometry	Constitutive modelling	Case analyzed and particular characteristics	Main emphasis
Habib (1967)	Heat induced by friction on a shear band, including heat losses.	Planar	N/A		Generated vapour pressure in the shearing band may explain a rapid motion
Romero and Molina (1974)	Dynamics of motion expressed as a balance of energy: slide deformation, basal friction, impulse of reservoir water and kinetic energy. Pore pressure determined in a phase diagram vapour-liquid water	Compound failure surface. Defined by vertical slices	Mohr-Coulomb	Vaiont. Run-out and velocity determined during the entire motion	Explaining the high velocity of Vaiont
Voigt and Faust (1982)	Rigid mass sliding and deformation concentration in a shear band Saturated shear band Terzaghi's effective stress Mass, energy and momentum balances One dimensional model for heat and pore water pressure dissipation.	Planar	Mohr-Coulomb	Vaiont. Average block. 1D Finite Element analysis	Heat induced fluid pressure explains Vaiont velocity
Vardoulakis (2000, 2002)	As in V&F(1982)	Slip circle	Mohr-Coulomb frictional strength	Vaiont.	Dynamic post failure response

	Numerical analysis		Shear strain and shear strain rate softening of frictional coefficient	Slide triggering by reducing the frictional angle from the strict equilibrium	
	Heat advective term negligible				
	No vapour generation		Thermal expansion coefficient of the soil skeleton including thermoelastic expansion and thermoplastic collapse		
Veveakis et al. (2007)	As in V&F(1982)	Planar	Mohr-Coulomb frictional strength	Vaiont.	Long creeping phase of Vaiont landslide and the final high acceleration due to the onset of thermal pressurization
	Analytical solutions		Thermal softening and velocity strengthening law for frictional coefficient	Slide triggering by reducing frictional angle from strict equilibrium	
			Thermal expansion coefficient of the soil skeleton including thermoelastic expansion and thermoplastic collapse	Constant water table in Veveakis et al. (2007)	
Goren & Aharonov (2007)	As in V&F(1982)	Planar	Mohr-Coulomb frictional strength	Synthetic cases	Long travel distances of landslides and their relation to slide volumes depending on the depth dependent permeability
	Numerical analysis		Constant frictional coefficient	Slide triggering by an initial velocity	
	Advective term and heat conduction negligible			Sensitivity analysis	
	No vapour generation				
Goren & Aharonov (2009)	As in V&F(1982)	Planar	Mohr-Coulomb frictional strength	Synthetic cases	Sensitivity analysis of the triggering factors and constitutive and geometrical parameters to evaluate the effect on the regime of the
	Numerical analysis		Constant frictional coefficient	Slide triggering by imposing an initial velocity (e.g. simulating an earthquake) and imposing an excess pore	
	Advective term and heat conduction negligible		Constant thermal expansion coefficient		
	No vapour generation				

				water pressure that dissipates in time (e.g. simulating rain of snow melt infiltration).	landslide which may become an arrested or catastrophic slide.
Pinyol and Alonso (2010a)	As in V&F(1982) Analytical solution Advective term and heat conduction negligible Incompressible water and soil skeleton No vapour generation	Planar	Mohr-Coulomb frictional strength Constant frictional coefficient Constant thermal expansion coefficient	Synthetic cases Slide triggering by increasing the water level	Analytical solution for the slide velocity. Sensitivity analysis of constitutive and geometrical parameters to evaluate the slide evolution.
Pinyol and Alonso (2010b)	As in V&F(1982) Numerical analysis Advective term and heat conduction negligible No vapour generation	Compound failure surface. Two interacting wedges describe evolving geometry	Mohr-Coulomb frictional strength Constant frictional coefficient Constant thermal expansion coefficient	Vaoint. Slide triggering by increasing the water reservoir level from the strict equilibrium	Dynamic post failure response. Sensitivity analysis of constitutive parameters and scale effects.
Goren et al (2010)	As in V&F(1982) Numerical analysis Advective term and heat conduction negligible No vapour generation	Planar sliding travelling along a surface not totally planar	Mohr-Coulomb frictional strength Constant frictional coefficient Constant thermal expansion coefficient Thermal decomposition of Dolomite which involve increments in porosity	The Heart Mountain landslide in Canada.	Simulation of the long runout features of the simulated landslides

			Non constant permeability		
Cecinato et al. (2011) Cecinato and Zervos (2012)	As in V&F(1982) Numerical analysis Heat advective term negligible	Planar and slip circle	Thermoplastic Modified Cam clay Strain, strain rate and temperature softening of the critical state parameter function of the friction angle at critical states Thermal expansion coefficient of the soil skeleton including thermoelastic expansion and thermoplastic collapse	Vaiont in Cecinato et al. (2011) Jiufenghershan landslide (Taiwan) in Cecinato and Zervos (2012)	Evaluation the effect of the thermal, strain and strain rate softening and the pressurization mechanism in Cecinato et al. (2011) Parametric analysis in Cecinato and Zervos (2012)
He et al. (2015)	As in V&F(1982) Numerical analysis Advective term and heat conduction negligible Depth-average integration model	Planar	Mohr-Coulomb frictional strength Constant frictional coefficient Constant thermal expansion coefficient	Synthetic case	A depth-averaged model coupled with a thermo-poro-elastic approach in the shear zone

Table 2. Material properties for water and solid particles

Parameter	Symbol	Value	Unit
Water			
Density	ρ_w	1,000	kg/m^3
Coefficient of compressibility	α_w	5×10^{-10}	1/Pa
Thermal expansion coefficient	β_w	3.42×10^{-4}	1/ºC
Specific heat	c_w	4.186×10^{3}	J/kg·ºC
Conductivity	Γ	0.580	J/m·s·ºC
Solid particles			
Density	ρ_s	2,700	kg/m^3
Thermal expansion coefficient	β_s	3×10^{-5}	1/ºC
Specific heat	c_s	8.372×10^{-2}	J/kg·ºC
Conductivity	Γ	0.375	J/m·s·ºC
Soil			
Porosity	n	0.2	-

Table 3. Typical ranges permeability, coefficient of compressibility and band thickness

Parameter	Symbol	Range of value	Unit
Permeability	k	$10^{-13}-10^{-5}$	m/s
Coefficient of compressibility	m_v	$10^{-10}-10^{-8}$	1/Pa

Shear band thickness	2*e*	0.001-0.05	M